Spring 1-1-2019

Computer Image Analysis Based Quantification of Comparative Ihc Levels of P53 And Signaling Associated With the Dna Damage Repair Pathway Discriminates Between Inflammatory And Dysplastic Cellular Atypia

Mark Richard Rutenberg
Cleveland State University

Recommended Citation

Rutenberg, Mark Richard, "Computer Image Analysis Based Quantification of Comparative Ihc Levels of P53 And Signaling Associated With the Dna Damage Repair Pathway Discriminates Between Inflammatory And Dysplastic Cellular Atypia" (2019). *ETD Archive*. 1268.
https://engagedscholarship.csuohio.edu/etdarchive/1268

COMPUTER IMAGE ANALYSIS BASED QUANTIFICATION OF COMPARATIVE IHC LEVELS OF

P53 AND SIGNALING ASSOCIATED WITH THE DNA DAMAGE REPAIR PATHWAY

DISCRIMINATES BETWEEN INFLAMMATORY AND DYSPLASTIC CELLULAR ATYPIA

MARK RICHARD RUTENBERG

Master of Science in Electrical Engineering

Cleveland State University

December 1986

Submitted in partial fulfillment of the requirements for the degree of

DOCTOR OF PHILISOPHY IN REGULATORY BIOLOGY

at the

CLEVELAND STATE UNIVERSITY

May 2020

We hereby approve of this dissertation for

Mark Richard Rutenberg

Candidate for the Doctor of Philosophy Degree

Department of Regulatory Biology

and

CLEVELAND STATE UNIVERSITY'S

College of Graduate Studies by:

_____ Date: _____

Dr. Crystal M. Weyman

Department of BGES, CSU, Committee Chair

_____ Date: _____

Dr. Valentin Böerner

Department of BGES, CSU

_____ Date: _____

Dr. Alex Almasen

Cancer Biology, Lerner Research Institute, CCF

_____ Date: _____

Dr. Roman Kondratov

Department of BGES, CSU

_____ Date: _____

Dr. Christine Moravec

Cardiovascular and Metabolic Sciences, Lerner Research Institute, CCF

_____ Date: _____

Dr. Aimin Zhou

Department of Chemistry, CSU

May 2, 2019

Student's Date of Defense

DEDICATION

This work is dedicated to the remarkable faculty of Cleveland State University that have, guided and taught me over the years and in particular to a remarkable educator, Dr. Crystal Weyman.

Many have commented on Dr. Weyman's exemplary dedication to her students and to the University, and she has already won every possible academic award in this regard.

In the course of both my education and my career I have come to know both clinicians and scientists and have had the opportunity to ponder on their essential commonalities and distinctions. I have found that the intellectual and emotional characteristics that seem to best define a scientist are creativity and curiosity, and I believe that those same two qualities of creativity and curiosity that have made Dr. Weyman a successful scientist have also resulted in her being such an exemplary educator of scientists.

From our first meeting it was clear that Crystal was curious about who I was intellectually and what my research interests were and could be, and was also continually creative in her guidance as to how to best encourage and develop both.

I believe that the faculty of very high-quality science departments at public universities like Cleveland State have an unusual opportunity to discover, develop, and encourage in their students an incipient scientific curiosity and creativity that may not have been previously apparent. I will be forever grateful to Dr. Weyman for doing exactly that for me.

COMPUTER IMAGE ANALYSIS BASED QUANTIFICATION OF COMPARATIVE IHC LEVELS OF

P53 AND SIGNALING ASSOCIATED WITH THE DNA DAMAGE REPAIR PATHWAY

DISCRIMINATES BETWEEN INFLAMMATORY AND DYSPLASTIC CELLULAR ATYPIA

MARK RICHARD RUTENBERG

ABSTRACT

Epithelial oncogenesis is believed to be generally associated with the accumulation over time of an increasing number of mitotic errors until a threshold number of mutations required for the initiation of cancer is achieved. Preemption of cancer through the morphologic detection of dysplastic cells, i.e. cells with a number of mitotic errors that are still below the threshold for cancer, followed by their surgical removal or eradication, has had an enormous impact on reducing the incidence of cancer of the uterine cervix, skin and colon worldwide, but this strategy has been much less successful with cancers in most other body sites. Inflammation is a relatively common occurrence in the epithelium and is far more common than cancer. A major current obstacle to the preemption of carcinoma is distinguishing morphologically atypical epithelial cells in the presence of inflammation (inflammatory atypia) that mimic dysplasia from morphologically atypical epithelial cells that are truly dysplastic. Formation of double stranded breaks in DNA (DSBs) is an accepted etiology for carcinoma and is, therefore, expected to be associated with dysplasia. Utilizing both algorithmic and artificial intelligence-based computer image analysis of IHC levels, we document the unexpected finding that phosphorylation of molecular markers associated with DSBs is consistently correlated with non-dysplastic

inflammatory atypia in both squamous (oral cavity) and glandular (Barrett's metaplasia) epithelia. Using these same image analysis methods, we further show that quantitative immunohistochemistry of the ratio of p-Chk2, a marker of DSB's, and for mutational failure of the DNA damage repair pathway (p53) required for the proper response to DSBs can distinguish between inflammatory and dysplastic cellular atypia. The ability to use quantitative means to reliably distinguish between inflammatory and dysplastic atypia may facilitate the use of cytological screening for dysplasia to prevent cancer in numerous body sites.

TABLE OF CONTENTS

LIST OF FIGURES

CHAPTER I

INTRODUCTION

1.1 The vast majority of cancers in adult humans are carcinomas. The presumed causality and epidemiology of carcinoma provides important evidence for the multi-hit theory of carcinogenesis.

Over 97% of adult human cancers, including cancers of the breast, cervix, uterus, bladder, prostate, lung, mouth, throat, nasopharynx, esophagus, stomach, pancreas, and colon are carcinomas (Siegel et al. 2019). As such, these cancers all originate in the approximately 500-micron thick epithelial tissue layer that lines each of these organs.

The presumed causality of this concentration of cancer in the epithelium provides strong indirect evidence for the multi-hit theory of carcinogenesis. Oncogenesis, in general, and carcinogenesis, in particular, are believed to be the result of the accumulation over time of approximately 6-8 individual DNA replication errors that randomly occur during individual mitosis. (Martincorena et al. 2017; Vogelstein and Kinzler 1993). Recent evidence suggests that the majority of these DNA replication errors are purely stochastic in nature and not related to the presence of any environmental carcinogens or inherited

mutations (Tomasetti et al. 2017). That is, most cancers are not related to lifestyle and environmental exposure, and only a small number are primarily due to genetic factors. The role of environmental carcinogens though, is thought to be limited to increasing the probability of a DNA replication error occurring during a mitosis that is concurrent with or subsequent to the carcinogenetic exposure.

The likelihood that the threshold minimum number of mitotic errors required for cancer will accumulate in one of the cells in a particular tissue over a specific time frame (i.e. the individual's life span) is, of course, dependent on the prevalence of mitosis in that specific tissue. The epithelium, due to its physiological role and anatomic structure, is a locus of mitosis and as a result, is a predominant locus of cancer.

Due to their role as an interface between the surface of a particular organ and its internal or external environment, epithelial tissues are nearly completely avascular. To protect the epithelium from routine mechanical abrasion, (i.e. shaking hands or eating a carrot), the metabolic requirements of epithelial cells are primarily satisfied through diffusion or transport of molecules across the basement membrane or lamina propria from the relatively perfuse blood and lymphatic circulation found in the underlying connective tissue (Gibbins 1972).

For this reason, epithelia have no more than an average thickness of 500 microns, as cells further removed from the submucosa would not be able to meet their metabolic requirements. To compensate for both their required thinness and continual exposure to mechanical and chemical insult from the immediate environment, epithelia are rapidly

and continually regenerated, with turnover of the entire 500μ epithelial layer occurring in as little as three days in some areas of the small intestine, to one week in the oral cavity, to three weeks in the esophagus, and a maximum of six weeks in the uterine cervix (Creamer et al 1961).

This large amount of epithelial turnover requires continual mitosis to replace exfoliated cells at the end of their short lifetime in the tissue. Stochastically, some of these numerous mitoses will entail a DNA replication error. If this replication error escapes the DNA error detection and repair mechanisms, then daughter cells will inherit the error and pass it along to their descendants establishing a clone of epithelial cells with one genetic error.

If, at a further point in time in the lifespan of the organism, one of the cells in this clone with one genetic error stochastically creates another replication error during a subsequent mitosis, which could occur months or years after the first error was created, a smaller clone of cells with two genetic errors will now be established within the larger clone of cells with one error from which it arose.

Given a high rate of mitosis in a tissue and sufficient time to accumulate genetic mutations resulting from those mitoses, the likelihood that a cell will ultimately accumulate the threshold minimum number of mutations required for cancer (approximately eight for most epithelia), increases. It is precisely these two factors that make the adult epithelium so susceptible to the development of cancer. In summary, the high rate of mitosis necessarily required for continual regeneration of epithelia combined

with the increasingly long human lifespan, together results in carcinomas, i.e. cancers arising from the epithelium, accounting for over 95% of all adult human cancers.

1.2 The discovery and clinical utility of morphologically defined dysplasia in cytological screening

1.2.1 Cytology of the uterine cervix

Until the 1960s, cervical cancer was the single largest cause of female cancer deaths in the US, all of North and South America, all of Europe, and all of Asia. By 1975, it had dropped to the 14th cause of female cancer deaths in the US with similar decreases worldwide (National Institute of Health 2010).

This remarkable achievement against a major cancer resulted from a discovery made by George Papanicolaou in the 1930s. Papanicolaou discovered that years before women presented with the typical initial symptoms of invasive cervical cancer, i.e. heavy inter-period bleeding and pain, they exfoliated from the surface of the squamous epithelium of their cervix a cell, which when fixed in alcohol and stained properly (with what later came to be known as the modified Papanicolaou stain), appeared in several characteristic ways to have an abnormal shape (morphology) under the light microscope. The nuclear to cytoplasmic ratio of these cells was higher than normal, and their nuclei were considerably darker. In addition, while normal squamous nuclei are round, the nuclei of these cells were more irregularly shaped, and while the appearance of chromatin

in normal nuclei is generally uniform, the chromatin in these cells appeared much more granular (Koss 1961).

Taken together, these characteristic morphologic features were named by Papanicolaou as "dysplasia" or "bad form". In general, Papanicolaou found that while the vast majority of cells exfoliated from the cervix and captured on "Pap smears" obtained from all women were normal, those few women who later developed cervical cancer had evidence of these "dysplastic" cells, (the ratio being about 50 abnormal to every 100,000 normal cells) while women whom he followed for years and did not have "dysplastic" cells, did not develop cervical cancer. The cervix is a relatively small organ, and therefore simple surgical techniques to destroy (ablate) the involved epithelium in women with "dysplastic" Pap smears, while maintaining their reproductive capacity, were readily developed in the 1960s. No other intervention to prevent, or better, to "preempt" any cancer has been as successful as screening for dysplastic cells and ablation of the cervical epithelium in women who displayed them. As precancerous lesions found by Pap smears can be treated and cured before they develop into cancer, the incidence and death rates for this disease are now remarkably low.

1.2.2 Oral cytology

By the mid-1970s, it was clear from the cervical cancer experience that cytological screening could have a major impact on preventing cancer in other organ systems, and it was therefore tried on several other easily accessible body sites including the oral cavity.

Oral cancer kills about as many Americans as melanoma, and while historically a disease of older male tobacco users, the incidence of oral cancer in women, young people, and non-smokers has been increasing rather dramatically in both the US and Europe over the last 30 years. (Paderno et al. 2018; Iype et al. 2001) .

In the 1960s and 1970s, several large studies of exfoliative oral cytology were conducted with disappointing results (Folsom et al. 1972; Sandler 1962). Unlike the uterine cervix, areas of dysplasia in the oral cavity are typically covered with a keratinized epithelium which prevents exfoliation of dysplastic cells to the surface, dramatically limiting the sensitivity of cytological screening. Furthermore, the rate of epithelial turnover in the oral cavity is significantly greater than the cervix, which results in greater exfoliation of normal cells, further diluting the number of abnormal cells on the cytology smear. (Hayes et al 1969).

Advances in the 1990s allowed computer-based image processing to detect rare abnormal cells scattered among a large number of normal cells (Mango and Radensky 1998). When this technology was combined with a transepithelial brush sampling technique in 2000, which allowed collection of cells below the keratin layer, the sensitivity of oral cytology was greatly improved. A study conducted at 35 academic centers utilizing computer-assisted analysis of a transepithelial oral cytology sample demonstrated a sensitivity of nearly 100% when compared to histologically confirmed oral dysplasia and cancer (Sciubba et al. 1991). Specificity of this technique however, was limited to 90%

resulting in a positive predictive value in this study and in subsequent studies of less than 40% for low grade dysplasia (Svirsky et al. 2002).

The specificity of oral cytology, particularly in the diagnosis of mild or low grade dysplasia, is limited by the fact that inflammation, which is quite common in the oral cavity, often causes morphologic changes to the cell (i.e. large nuclear to cytoplasmic ratio, hyperchromicity, lack of nuclear roundness, and chromatin granularity) that can appear identical to the morphologic changes associated with precancerous dysplasia.

The difficulty in making a morphologically based diagnosis of Inflammation vs dysplasia in oral cytology is illustrated in Figure 1.

A molecular method to help distinguish true "dysplastic atypia" from similarly appearing "inflammatory atypia" would be of significant benefit in enhancing the clinical utility of transepithelial oral cytology to help prevent this typically fatal cancer.
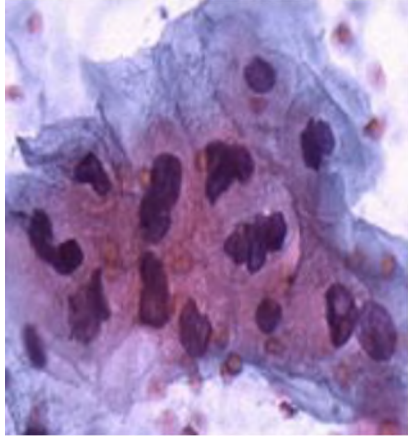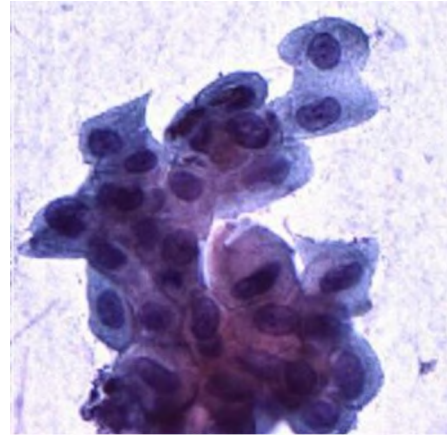
(a)   (b)

Figure 1. Dysplastic (a) and inflammatory (b) squamous cytological atypia have a morphologically similar appearance. Note the similar nuclear/cytoplasmic ratio, chromatic granularity, and darkness, and non-circular shape of the nucleus that is found in both dysplastic and inflammatory change as these are the characteristic morphologic signs of dysplasia. Transepithelial cytology specimens of oral leucoplakias, stained with modified Papanicolaou, 100X.

1.2.3 Esophageal cytology

Esophageal adenocarcinoma, thought to be the result of chronic reflux of excess stomach acid into the esophagus, is the most rapidly growing cancer in the U.S. and Europe, and one of the most fatal (Rustgi and El-Serag 2014).

In an effort to identify esophageal dysplasia before it can progress into cancer, gastroenterologists obtain random tissue samples of the esophagus during upper endoscopies from patients with gastroesophageal reflux disease (GERD) and Barrett's esophagus (BE), a metaplastic precancerous change induced by GERD.

Esophageal dysplasia is usually invisible to the naked eye endoscopically and furthermore, dysplasia is typically highly focal, occurring in only microscopic portions of mucosa within a large area of BE (Sharma 2004). Consequently, current guidelines from the American College of Gastroenterology (ACG), American Gastroenterological Association (AGA) and American Society for Gastrointestinal Endoscopy (ASGE) recommend that gastroenterologists employ an aggressive biopsy protocol by obtaining random 4-quadrant forceps biopsies from every 1 – 2 centimeters of BE combined with targeting suspicious areas that are visible to the naked eye at endoscopy (the "Seattle protocol"). Unfortunately, even with the use of this sampling protocol, up to 96% of the endoscopically suspect area of BE remains completely unsampled in most patients (Smith 2016). Since dysplasia is usually focal in its location, and inconspicuous and macroscopically indistinguishable from the surrounding tissue, random 4-quadrant forceps biopsies often fail to sample the precise area of disease that is being investigated

and thus, often misses abnormalities that are located between sampled areas (Spechler 2002; Visrodia et al. 2016). This results in significant sampling error and false negative results (Sharma 2004).

To overcome sampling error, and in light of the success of uterine cytology (the Pap smear), superficial exfoliative cytology of the esophagus was attempted and eventually adopted by approximately 17% of gastroenterologists by 2000 (Falk 2003). However, like cytology of the oral cavity, esophageal cytology suffers from low sensitivity (Kumaravel et al. 2010). This is primarily due to the fact that metaplastic glandular epithelium associated with Barrett's esophagus does not exfoliate dysplastic cells to the glandular surface, unlike the readily exfoliating squamous epithelium of the cervix.

This poor sensitivity of esophageal cytology was overcome in 2011 with the introduction of an abrasive brush, which obtains a wide area transepithelial cytological specimen that reaches the submucosa, combined with computer-assisted analysis of that sample to detect rare dysplastic cells found in the thick transepithelial cytological sample. (Johanson et al. 2011; Anandasabapathy et al. 2011).

While high grade dysplasia and early cancer are readily identified cytologically (Kumaravel et al. 2010), as in the oral cavity, the specificity of transepithelial esophageal cytology is limited by the fact that inflammatory cellular atypia can be morphologically indistinguishable from atypia associated with low grade dysplasia (Figure 2). This is especially problematic for esophageal patients with GERD symptoms being evaluated for

dysplasia, as inflammation caused by their acid and bile reflux is frequently identified during endoscopy.

As a result, most pathology laboratories will commonly report cases that exhibit inflammation as "indefinite for dysplasia" even though the very same case displays pronounced morphologic cellular atypia. Molecular differentiation of these morphologically similar entities would thus enhance the utility of wide area transepithelial cytological testing of patients with known or suspected Barrett's esophagus.
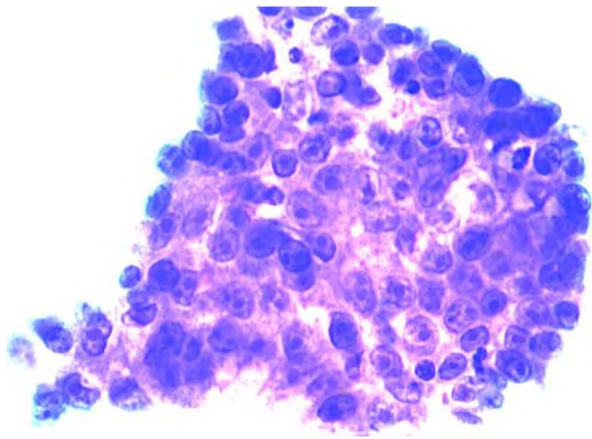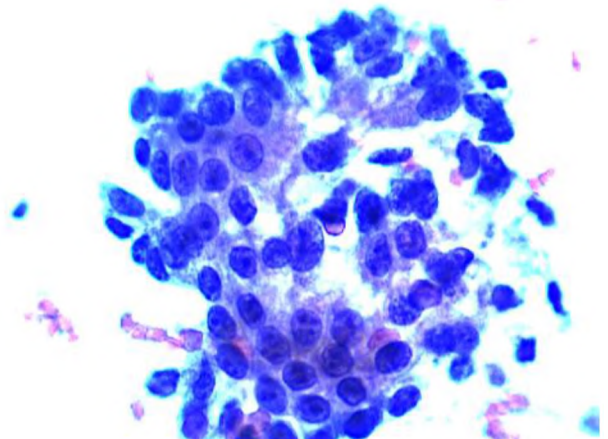
(a)   (b)

Figure 2. Dysplastic (a) and inflammatory (b) glandular cytological atypia have a morphologically similar appearance. Note the similar chromatic granularity and nuclear darkness and the non-circular shape of the nucleus found in both dysplastic and inflammatory change as these are the characteristic morphologic signs of dysplasia. Transepithelial cytology specimens of Barrett's esophagus, stained with H&E, 100X.

1.3 Correlation between the Molecular and Morphological Definitions of Dysplasia

Anatomic pathology consists of a series of correlations between the morphological appearance of cells and/or tissue and a known disease state or clinical outcome. In the 1930s, when Papanicolaou discovered that abnormally shaped cells in healthy women preceded the appearance of invasive cervical cancer in these same women by many years, molecular biology as a science did not yet exist, and there was no understanding of the molecular basis of oncogenesis.

Screening colonoscopy to detect and excise dysplastic polyps before they progress to cancer became part of routine clinical care in the late 1980s and coincided with the rapid advancement of molecular techniques to detect abnormal genes and gene products.

Epithelial cancers (i.e. carcinomas) are generally believed to develop by a multistep process during which a normal epithelial cell accumulates an increasing number of uncorrected mitotic errors over time such that it progresses to premalignant low-grade dysplasia, to premalignant high-grade dysplasia, to carcinoma in situ and then to invasive cancer (Naini et al. 2016).

With regard to sporadic colon cancer, for patients at high risk, screening for dysplastic polyps will often be recommended at a younger age than for patients with no risk factors, and intervals between subsequent colonoscopies will vary significantly depending upon whether dysplastic or non-dysplastic polyps were found on the initial colonoscopy. As a matter of course therefore, polyps that may be endoscopically

identified and removed during colonoscopy from a screening population will upon pathological examination represent the entire morphologic spectrum of oncogenesis from non-dysplastic adenoma, low grade dysplasia, high grade dysplasia, carcinoma in situ, and cancer. Once dysplasia is diagnosed, progression towards malignancy is dramatically increased and therefore, careful surveillance is warranted (Wani et al. 2011).

A thorough understanding of the molecular basis of the origin and progression of morphologically described dysplasia to cancer was first ascertained through molecular analysis of polyps removed during routine screening colonoscopy.

The landmark study by Vogelstein and Kinzler on polyps removed during colonoscopy demonstrated that dysplasia was characterized on the molecular level by an accumulation over time of genetic abnormalities responsible for controlling cell division and/or differentiation. Further studies have confirmed that what was morphologically described as low-grade dysplasia was associated with 2-3 such genetic mutations, while high grade dysplasia was associated with 3-7 mutations, and cancer was typically associated with 8 or more mutations.

A similar correlation between the number of deleterious genetic mutations in a cell and the degree of morphologically described dysplasia has been corroborated in every carcinoma in which it has been studied (Contino et al. 2017; Vogelstein and Kinzler 1993; Weinberg et al. 2018).

1.4 Inflammation predisposing to oncogenesis as a "two-hit" causality phenomenon

The clinical correlation between chronic inflammation and increased susceptibility to carcinoma has been well demonstrated in several body sites, most notably in the lung and in the colon of patients with inflammatory bowel disease (Gomes et al. 2014; Gupta et al. 2007).

Since inflammation is very common and carcinoma is relatively rare, this clinical correlation may represent a special case of the "multi-hit" theory of carcinogenesis first proposed by geneticist Alfred Knudson in 1971, and is usually associated with the accumulation of genetic mutations over time as discussed above. Today, this hypothesis serves as the basis for understanding how mutations in tumor suppressor genes contribute to the development of cancer. Thus, chronic inflammation may predispose a cell to oncogenesis that requires a second stochastic event.

1.4.1 Overview of inflammatory mechanisms potentially related to carcinogenesis

There is strong evidence supported by cumulative clinical and epidemiological studies that inflammation increases the risk of human cancers in almost all epithelia.

A chronically-inflamed environment is characterized by the presence of heterogeneous inflammatory cellular components, which produce growth stimulating mediators (inflammatory cytokines and growth factors), chemotactic factors (chemokines) and genotoxic substances (reactive oxygen species and nitrogen oxide) and

induce DNA damage and methylation (Kanda et al. 2017). This is especially evident in patients with low-grade chronic inflammation (Murata et al. 2012).

Inflammation-related carcinogenesis is most commonly associated with infectious agents induced by certain viruses, bacteria, or parasites. In fact, it has been estimated that 20% of all cases of cancer worldwide are caused by infections including human papillomavirus associated with cervical and anal cancer, *Helicobacter pylori* infection associated with stomach cancer, *Schistosoma haematobium* infection associated with bladder cancer, and chronic hepatitis B and C viruses and fluke infections with liver cancers (Ohnishi et al. 2013). A wide array of chronic inflammatory conditions that are noninfectious in etiology predispose susceptible cells to neoplastic transformation and account for approximately 25% of all human cancers (Hussain and Harris 2007). For example, autoimmune diseases such as inflammatory bowel disease is strongly associated with development of colorectal cancer, Barrett's esophagus has been demonstrated to be the only established precursor to esophageal adenocarcinoma, and foreign bodies which cause inflammation, such as cigarette smoke, and asbestos or other fine particulate matter in the air, are associated with lung cancer and malignant pleural mesotheliomas respectively (Kanda et al. 2017).

Inflammatory cells secrete a large number of cytokines (tumor necrosis factor (TNF), interleukins) and chemokines (CCL2 and CXCL8) that promote the outgrowth of neoplastic cells, in addition to the growth factor production by the tumor cells themselves (Dinarello 2007). Under the stimulus of pro-inflammatory cytokines in phagocytic and

non-phagocytic cells, reactive oxygen species (ROS) and reactive nitrogen species (RNS) are generated and are capable of causing damage to various cellular constituents including nucleic acids, proteins, and lipids (Ohnishi et al. 2013). The DNA damage caused by ROS and RNS results in mutations, the accumulation of genetic alterations in tissues, and increased cell proliferation which have been implicated in the initiation and/or promotion of inflammation-mediated carcinogenesis (Kawanishi et al.) Stem cells damaged by ROS/RNS from inflammation can generate cancer stem cells and ultimately, cancers with aggressive clinical features (Thanan et al. 2013).

Recently, inflammation-driven carcinogenesis has been shown to be mediated through STING (Stimulator of Interferon (IFN) Genes) a cellular sensor that has been shown to trigger the expression of select cytokines that in turn bind receptors signaling for the production of pro-inflammatory cytokines (Ahn et al. 2014). Controlling STING-dependent cytokine production may provide a basis for therapeutic strategies to help prevent malignant disease.

The association of inflammation and cancer has been most carefully studied in the colon. As with other inflammatory conditions, chronic inflammation of the colon can contribute to carcinogenesis by increasing oxidative stress and DNA methylation, which results in inhibition of oncosuppressor genes, mutation of p53, aneuploidy, and microsatellite instability (Scarpa et al. 2014). It is now well established that the molecular alterations responsible for sporadic colorectal cancer also play a role in colitis-associated colon carcinogenesis (Gupta et al. 2007). The strong link between colon inflammation and

cancer is further supported by the fact that colorectal cancer risk increases with a longer duration of colitis, a greater extent of colitis, a concomitant presence of other inflammatory manifestations such as primary sclerosing cholangitis, and also the fact that drugs used to treat inflammation may prevent the development of colon cancer (Triantafillidis et al. 2007).

1.4.2 Inflammation induced DSBs

Double-strand breaks in DNA (DSBs), in which both strands in the double helix are severed, are particularly hazardous to the cell because they can result in genomic rearrangements. Inaccurate DNA repair can lead to mutations and/or chromosomal aberrations that can result in the development of cancers (Bartkova et al. 2005). In response to sensing DSBs, cells initiate a DNA damage response (DDR) that activates DNA repair pathways, which include the activation of different transcription programs, cell cycle checkpoints to induce transient or permanent cell cycle arrest (senescence), activation of specific repair pathways and apoptosis if repair fails (Jeggo and Lobrich 2007). Prolonged inflammation by infection or autoimmune diseases results in reduced repair capacity, launching more reactive oxygen species (ROS) and subsequent oxidative DNA damage, which in turn induces further inflammation in intact distant cells as stress signals as well as exacerbation of DNA damage, which lead to carcinogenesis (Mittal et al. 2014).

Barash et al. (2010) and others (Kiraly et al. 2015) noted the association of chronic inflammation-induced double-strand DNA breaks with accelerated carcinogenesis following liver regeneration. In their study using a mouse model, they demonstrated that the regenerative proliferative stress induced by liver resection resulted in genomically unstable hepatocytes which were generated during chronic inflammation escaping senescence or apoptosis and reentering the cell cycle, triggering enhanced tumorigenesis.

The discovery of *Helicobacter pylori* as the causative agent of peptic ulcer disease has led to an increased understanding of the connection between chronic infection, inflammation, and cancer. *H. pylori* infection induces the formation of DSBs directly through host–pathogen contact or indirectly due to the accompanying chronic inflammation, eventually triggering the DDR pathway as assessed by the phosphorylation of H2AX (Toller et al. 2011). The integrity of DDR is compromised by various proteins of the DDR pathway which lead to a vicious cycle of DNA damage and persistent inflammation. Despite the fact that DSBs due to *H. pylori* are continuously being repaired, persistent infection and recurrent inflammation increases the likelihood that if p53 is mutated in the same cell that a DNA DSB will result in genetic instability and tumorigenesis (Kalisperati et al. 2017).

1.5   Molecular markers associated with DSBs

Double- strand DNA breaks (DSBs) are generally lethal to the cell, and as already noted, if not repaired prior to mitosis, will lead to genomic instability and tumorigenesis

that can be lethal to the organism. As a result, a complex and robust DNA Damage Repair (DDR) system to prevent unrepaired DNA from replication and completion of mitosis has been highly conserved. Detection of the phosphorylated state of those molecules within the DDR system that are responsible for detection of DSBs and prevention of mitosis prior to DNA repair can be utilized to infer the presence of DSBs (Jackson and Bartek 2009). The primary pathway engaged in the detection and response to DSB includes ATM, H2AX, CHk2, and p53 (Cao et al. 2006; Kang J et al. 2005).

To be effective in protecting the genome from instability, response to the detection of DSBs must be extremely rapid and the requirement to prevent a single mitosis of the broken DNA, absolute. This is because once broken DNA is allowed to be transmitted through mitosis and the mutated daughter cells may no longer contain intact DDR mechanisms to correct the original and subsequent DNA defect. Consequently, there may no longer be any regulatory control to block genomic instability.

To insure rapidity of response to DSBs, ATM, a serine/threonine protein kinase, self-phosphorylates upon detection of a DSB. A complex of three proteins MRE11, RAD50, and NBS1, (known as the MRN complex) recruits ATM to the DSB (Paull and Deshpande 2014).

 As a component of its rapid response to the detection of a DSB, p-ATM in turn phosphorylates CHk2 on the priming site T68 and on other residues in the SQ/TQ cluster domain (Zannini et al. 2014). Activated CHk2 then phosphorylates phosphatase CDC25A

causing its degradation. As a result of this degradation, CDC25A can no longer dephosphorylate CDK1-cyclin B resulting in immediate cell cycle arrest.

Interaction of ATM with NBS1 phosphorylates the histone H2AX on serine 139 forming γH2AX (i.e. p-H2AX). The exact role of γH2AX in DSB repair is under investigation but it appears that the phosphorylation results in the DNA which would otherwise be tightly wrapped around this histone to become less condensed facilitating its interaction with proteins necessary for repair of the DSB. While there is evidence that low levels of γH2AX may be associated with physiological processes unrelated to DSBs (Ryback et al. 2016), high levels of γH2AX can be detected as soon as 20 seconds after ionizing radiation. Maximum levels are recorded within one minute with chromatin, including γH2AX then extending to about a million base pairs on either side of the DSB (Rogakou et al. 1998).

If the DSB cannot be repaired during this rapid response phase, phosphorylation of Chk2 also results in the phosphorylation of p53 resulting in both its stabilization and activation. Activated p53 in turn results in transcription of several p53 target genes including CDK inhibitor p21 which leads to long term cell cycle arrest and/or apoptosis.

1.6   Use of mutated p53 as a molecular marker of dysplasia and carcinoma

The preeminent role of p53 in preventing the mitotic replication of cells with damaged DNA, and the consequent strong association of p53 mutation with oncogenesis is well known (Williams et al. 2016).

The level of wild type p53 is normally maintained at a low level in the cell by ubiquitin targeting and subsequent degradation (Brooks and Gu 2011). At this low physiological level, p53 is not typically detectible on IHC. Upon phosphorylation of upstream components of the DDR pathway in response to DSBs, particularly Chk2, wild type p53 is phosphorylated both activating and stabilizing the molecule. This stabilization of wild type p53 associated with its phosphorylation typically results in qualitative IHC pathology reports of a "low level of p53" or "moderately elevated level of p53".

As a quaternary protein, p53 is highly subject to dominant negative mutation. Consequences of p53 mutation include loss of its cell cycle control function and insensitivity to ubiquitin targeting for subsequent degradation (Rivlin et al. 2011). Since it is not being degraded, mutated p53 builds up in the cell to high levels that are easily detectible on IHC. Thus, the qualitative report of the clinical pathologist examining a histologic section of a tumor as "strongly positive for p53" is in most cases actually reflecting the detection of an accumulation of mutated p53.

In standard clinical pathology practice, the assessment of IHC is based on visually appreciating the number of stained cells and the intensity of the stain microscopically, indicating the relative number of molecules with the specific antigen that is being tested for. This qualitative assessment is subject to considerable inter-observer and intra-observer variability and considerable overlap in the reporting of low, moderate and high levels of p53 positivity.

While frank carcinoma is usually associated with an unmistakable, very highly positive p53 result on IHC, this is not often the case with the intermediate level of mutated p53, associated with both inflammatory and precancerous dysplasia. Visual subjectivity and lack of repeatability is particularly an issue in the differentiation between the low level of IHC positivity associated with the phosphorylation of wild type p53, and the higher level of p53 associated with mutated p53 in precancerous dysplasia.

In this study examining the potential role of DSBs in the development of carcinoma and the detection of precancerous dysplasia, computer based quantitative measurement of the level of p53 is used to differentiate between the detection of the phosphorylation of wild type p53 associated with its normal response to DSB, and the detection of mutated p53 associated with precancerous dysplasia and consequent failure to provide the normal cell cycle control response to DSBs.

CHAPTER II

MATERIALS AND METHODS

2.1   Computer-Assisted Transepithelial Brush Biopsy

2.1.1   Application to the oral cavity

Computer-assisted transepithelial oral brush cytology (OralCDx), is an in-office, noninvasive, painless, test that is performed by dentists and physicians to ensure that routine appearing white or red tissue changes (leukoplakia and erythroplakia) in a patient's mouth are not precancerous or cancerous. Its clinical role is thus to confirm the benign nature of those lesions that clinically appear to be benign, and more importantly, identifies precancerous and cancerous lesions when they are not suspected of being harmful.

The test consists of a transepithelial brush (Figure 3) that in contrast to a standard cytology instrument, which samples only the superficial epithelial layer and the surrounding mucous, the OralCDx brush obtains a complete tissue sample from the full thickness of the epithelium through the basement membrane under the oral lesion being tested.

Figure 3: A transepithelial oral brush biopsy instrument obtains a full thickness sample of the entire epithelium Unlike standard cytological sampling instruments that are designed to obtain a superficial sample of naturally exfoliated cells and/or organisms, a transepithelial oral brush biopsy instrument has sufficient tangent modulus (stiffness) to obtain a full thickness sample of the entire 500μ depth of the epithelium through and below the epithelial basement membrane.

Specimens obtained by this novel sampling technique are subjected to three-dimensional computer-assisted laboratory analysis as described below.

The high sensitivity of this method has been established in well designed, double blind studies (Sciubba et al. 1991; Mehrotra et al. 2011; Scheifele et al. 2004).

For example, in one of the largest studies in oral medicine ever conducted, performed at 35 academic centers in the U.S. and involving nearly 1,000 patients (Sciubba et al. 1991), OralCDx was demonstrated to have a sensitivity of greater than 96% and a specificity of greater 90%.

As shown in that study, nearly 5% of clinically benign-appearing lesions, which academic experts in oral medicine determined did not require a biopsy, were sampled by OralCDx, found to be dysplastic or cancerous, and then independently confirmed by a subsequent scalpel biopsy taken during the same examination to represent dysplasia or invasive cancer. Subsequent studies by Mehrotra et al. (2011) and Scheifele et al. (2004) confirmed the high sensitivity of OralCDx as demonstrated by Sciubba et al. (1991). In fact, in every published study in which oral lesions were subjected to both OralCDx and scalpel biopsy concomitantly, OralCDx was found to have a sensitivity of greater than 90% in identifying dysplasia and carcinoma. The method has been found to be particularly useful for the evaluation of minimally suspicious lesions that normally would otherwise not be subjected to scalpel biopsy, making it an effective test to evaluate the entire spectrum of lesions detected during an office-based oral cancer screening examination (Mehrotra et al. 2011).

Early assessment of oral and oropharyngeal abnormalities using this method, which include white, red, and mixed red and white lesions, has been shown to lead to prompt identification of dysplastic and early oral cancer, with better survival rates. In a study utilizing OralCDx to identify 102 patients with oral cancers that were predominantly asymptomatic, subtle, innocuous-appearing and difficult to diagnose, the 5-year survival of those patients was 94%, a figure significantly greater than reported in the literature for early stage oral cancers (Sciubba and Larian 2018). In this study, the results of the OralCDx test altered the health care provider's clinical evaluation and treatment of these 102 patients and ultimately had a significant impact on patient outcome. Professional delay, one of the major barriers to achieving early stage diagnosis of oral cancer, can potentially be overcome thereby decreasing morbidity and mortality associated with this disease.

Despite its high sensitivity, the transepithelial oral brush biopsy would benefit from improvements to its specificity and positive predictive value. The vast majority (>97%) of benign appearing oral lesions are in fact not dysplastic and are caused by inflammation. Thus, the limitation on the specificity of cytology caused by the morphologic similarity in appearance between inflammatory and dysplastic atypia noted herein limits the applicability of this method.

2.1.2 Application to the esophagus

WATS^{3D} (for Wide Area Transepithelial Sample with computer-assisted three-dimensional analysis of the resultant thick cytological specimen) is an adjunct to the

random four-quadrant forceps biopsy protocol (Seattle protocol). WATS[3D] was designed

to overcome the two most significant limitations of the Seattle protocol: 1) sampling error

which results in failure to identify patients with dysplasia and early stage cancers and 2)

poor pathological agreement in the interpretation of specimens which results in patients

receiving improper diagnoses and treatment.

The WATS[3D] procedure begins with the use of a transepithelial brush during

endoscopy (Figure 4), which is designed to obtain a Wide Area Transepithelial Sample of

the BE segment, including parts of the esophagus that would normally have remained

unsampled with small random forceps biopsies. The WATS brush samples a large

circumferential mucosal area of the esophagus and is also designed to sample the entre

500 micron thick glandular epithelium comprising the Barrett's segment, specifically

obtaining cells from the deep layers of the epithelium (deep crypts) where dysplasia

develops initially. WATS[3D] specimens are typically quite abundant with tissue and when

deposited on the slide consists mainly of tissue fragments that are much thicker (typically

up to 150 -200 microns thick) than conventional soft brush cytology specimens, the latter

of which consist mostly of single cells and small clusters of cells (less than 10 microns

thick), from only the superficial layers of the esophageal epithelium. WATS[3D] tissue

fragments consist of compact sheets of cells, large cohesive clusters of cells, and even

entire crypts that have unique three-dimensionality to the tissue.

Figure 4: An endoscopic brush designed to detect dysplasia in Barrett's esophagus samples the full 500μ thickness of the suspect epithelium. Unlike standard esophageal cytology instruments which obtain only superficial exfoliated cells and are typically used to test for the presence of microorganisms, an endoscopic brush that is designed to detect dysplasia in Barrett's esophagus uses a much more abrasive brush which samples the full 500μ thickness of the suspect epithelium.

The WATS[3D] specimens are analyzed by pathologists with assistance from a specialized three-dimensional (3D) computer analysis system that uses neural networks and artificial intelligence to identify abnormal cells and present them to the pathologist more of their natural in vivo appearance.

In terms of improving the pathologic analysis of esophageal specimens, the computer-assisted histologic and cytological analysis of WATS[3D] specimens (combined with immunohistochemistry when indicated) has been shown to greatly reduce inter-observer variability in establishing an accurate diagnosis of dysplasia by pathologists. The analytic validity of WATS has been tested and confirmed in a previously published study by Vennalagant et al. in 2015 in which the inter-observer agreement rate among pathologists analyzing WATS[3D] specimens using expert computer-assisted three-dimensional analysis of tissue specimens found substantial agreement amongst pathologists for diagnosis of low-grade dysplasia, high grade dysplasia and BE without dysplasia, with an overall kappa value 0.86 (95% CI 0.75-0.97). As a kappa value of 0.81–0.99 is regarded as "almost perfect agreement", the results of this study demonstrate that WATS[3D] results are reliable and reproducible in contrast to the poor agreement in assessing the presence and grading of esophageal dysplasia in forceps biopsies specimens, in which kappa values typically range from 0.2-0.5. (Kerkhof et al 2007; Montgomery et al. 2001).

The clinical validity of WATS[3D] has been tested and confirmed in 5 prospective published studies that have shown a significantly increased rate of detection of BE,

dysplasia and adenocarcinoma when used adjunctively to the Seattle protocol, effectively showing a much lower rate of sampling error.

For instance, Johanson et al. (2011) conducted a multicenter prospective clinical trial of 1,266 patients being screened for BE at 8 community-based gastroenterology sites and reported that the addition of WATS[3D] to targeted and random 4-quadrant FB increased the detection of BE by 39.8% (95% CI 32–48%). In a second multicenter prospective study conducted at 4 major academic centers involving 151 patients in a high-risk dysplasia surveillance program, Anandasabapathy et al. (2011) demonstrated that the addition of WATS[3D] to the Seattle protocol increased the detection of dysplasia by 42% (95% CI: 20.7–72.7).

More recently, three WATS[3D] studies were conducted using a larger and improved sampling brush, and a significantly enhanced three dimensional computer analysis system that increased the effective depth of field from 30 microns to 150 microns. For instance, in a multicenter prospective study by Vennagalanti et al. (2018) conducted at 16 major academic centers nationwide involving 160 patients with BE under surveillance, WATS[3D] detected an additional 23 cases of high grade dysplasia / esophageal adenocarcinoma missed by the Seattle protocol. In this study, WATS[3D] was four times more effective at detecting high grade dysplasia and esophageal adenocarcinoma compared to the Seattle protocol that utilized only forceps biopsies.

In another multicenter prospective trial by Gross et al. in 2018, 4203 patients screened for suspected BE, and those with known BE undergoing surveillance at 25

community-based practices underwent WATS[3D] adjunctively to targeted FB and random 4-quadrant FB. In that study, the authors reported that WATS[3D] increased the overall detection of BE by 83% (95% CI: 74% - 93%) and low grade dysplasia (LGD) by 88.5% (CI: 48% - 160%).

Finally, in the largest study to date using WATS[3D] to diagnose BE, dysplasia and cancer, 58 endoscopists at 21 sites enrolled 12,899 patients undergoing screening and surveillance, and confirmed that WATS[3D] markedly improved the detection of dysplasia by 242% (95% CI: 191%-315%) and BE by 153% (95% CI: 144-162%) (Smith et al. 2018). All of these studies clearly demonstrate that sampling error (which is common with random 4-quadrant forceps biopsies utilized in the Seattle protocol) can be greatly reduced with WATS[3D] with the potential to overcome the inherent limitations associated with current standard screening and surveillance techniques.

However, as with transepithelial sampling of the oral cavity, the incidence of inflammation of the esophagus dwarfs that of dysplasia and this the morphologic resemblance between inflammatory and dysplastic atypia continues to limit specificity and positive predictive value.

2.2 Immunohistochemistry (IHC) - Qualitative

Histopathologic diagnosis is primarily based on the architecture of a thin sliced tissue section following its preparation with a standard hematoxylin and eosin stain. Since

the mid 1990's cytopathology, the more detailed study of individual cells and/or cell clusters compensates for its lack of architectural information by supplementing cellular morphology with molecular testing.

Supplemental molecular information is generally obtained by any one of IHC, flow cytometry or FISH.

IHC is usually the first choice for routine testing of solid tissue biopsies and cytology. This is due to its ease of implementation, low cost, and most importantly the fact that the cellular morphology is generally preserve through IHC process, allowing for molecular and morphologic correlation on an individual cell. marker for the secondary antibody can be observed.

The major disadvantage of IHC compared to the other two techniques is that its interpretation is highly qualitative.

At the clinician's office, a portion of the transepithelial cytological specimen was deposited in formalin and shipped to the laboratory. At the laboratory, this specimen was centrifuged into a pellet "cell block" which was then embedded in paraffin so that it could be cut with the microtome into 3-4 micron sections. Each of these tissue sections or "cuts" was then stained with the respective IHC stain.

Immunohistochemical staining was performed on these FFPE sections using the Leica Bond max system (Leica Biosystems Newcastle Ltd, UK). Sections were dewaxed and pretreated with epitope-retrieval solution (ER, Leica Biosystems Newcastle Ltd, UK)

followed by 30 minutes of incubation with the primary antibody. The Leica Refine HRP kit (Leica Biosystems Newcastle Ltd, UK) was used for detection and counter-stained with Hematoxylin.

Evidence for the marker attached to the secondary antibody (DAB-HRP) was then manually searched for using a standard laboratory microscope, with both the intensity of the stain and the number of cells stained informally combined into an overall qualitative assessment (usually scored as 1-4) made by the pathologist using a manual microscope.

While this standard highly qualitative IHC method can detect major differences in IHC stain reaction it cannot reliably detect the subtler differences that would provide evidence of an inflammatory vs a dysplastic level of an IHC stain. The qualitative IHC response pattern for inflammatory and dysplastic atypia for the molecular markers that are the focus of this quantitative investigation is shown in Figure 5 which also illustrates qualitative similarity in appearance of the IHC response to both inflammatory and dysplastic atypia.
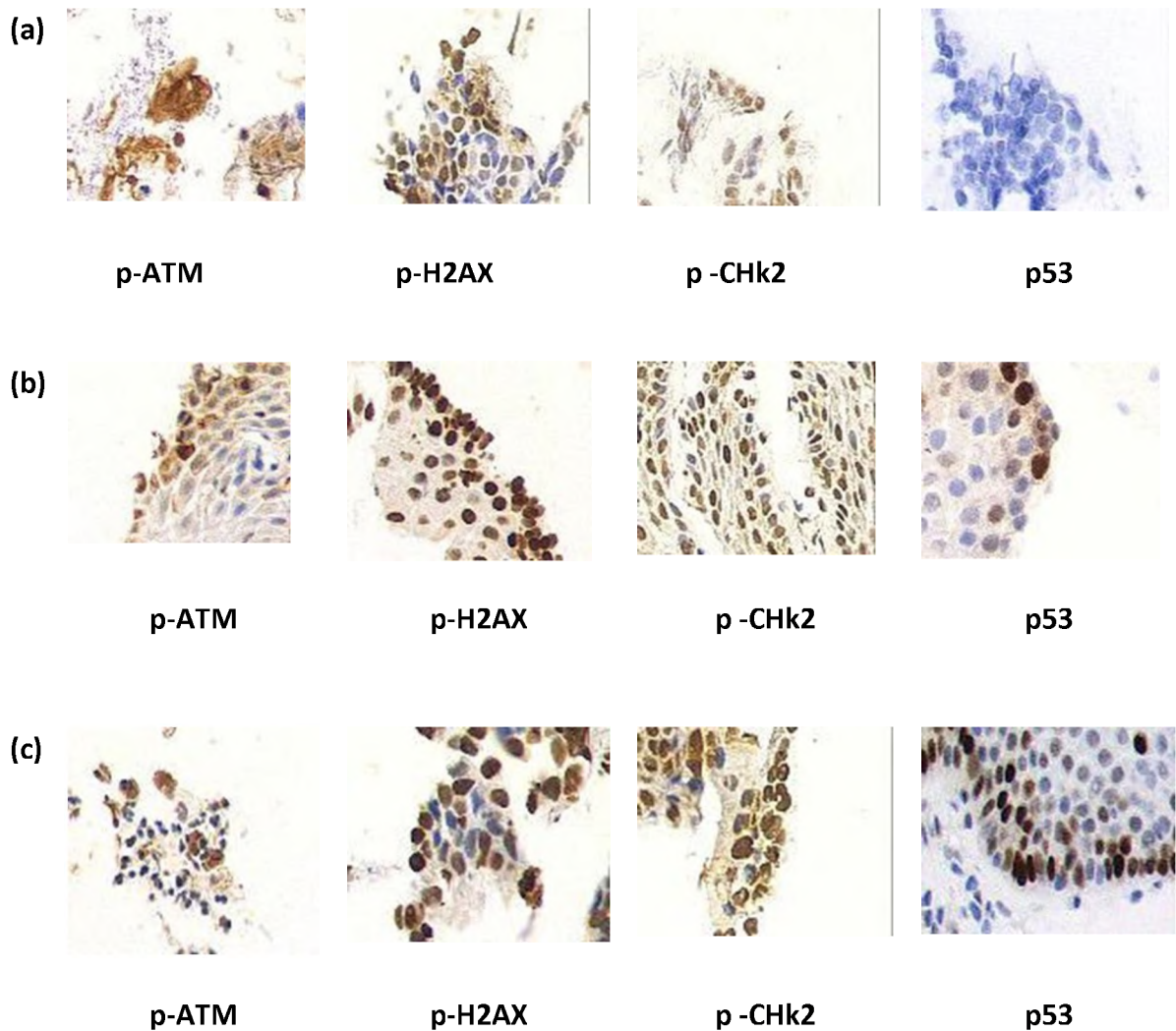
Figure 5: There is a strong qualitative similarity in the IHC response pattern to inflammatory and dysplastic atypia. In contrast to the IHC response pattern of tissue that is negative for both inflammation and for dysplasia (a) there is a strong qualitative similarity in the IHC response pattern to inflammatory atypia (b) and dysplastic atypia (c). Transepithelial cytology specimens of Barrett's Esophagus were centrifuged into a pellet which was paraffin embedded, sliced, and stained with the respective IHC antigen, 100X.

2.3 Computer-assisted quantitative analysis of IHC levels on transepithelial brush biopsy specimens

Quantitative analysis of IHC levels was developed for this study in order to overcome the limitations illustrated in Figure 4 of subjective qualitative analysis to the detection of detect subtle differences in stain response.

To accomplish this technological goal several limitations of standard algorithmic computer image processing had to be overcome.

Because the source of the specimen in this study was cytologic (individual cells and cell clusters removed from the sampling and centrifuged into a "cell block") and not histologic (intact tissue architecture), the resulting tissue cut is complex and partially three dimensional with numerous touching and overlapping cells.

Quantitative analysis of the IHC levels in these specimens requires: 1) differentiating non-epithelial artifacts, which may happen to stain, from actual epithelial cells, which properly evidence true antigenic response; and 2) differentiating individual cell nuclei and cytoplasmic boundaries from partially overlapping cells. If that latter is not properly done, then a low level of IHC stain intensity in two partially overlapping cells will falsely mimic a high level of stain intensity.

Standard computer image analysis is only performed algorithmically. That is, a computer program executes the measurement of predefined parameters to categorize the object. Thus an image processing system used to sort objects based on size or shape

would take predefined measurements of the object to achieve its predetermined sorting goal. This algorithmic sorting process generally requires that the objects being measured be separated in space. This is because once even two objects are allowed to touch or overlap, there are an infinite variety of ways that they can appear, and determination of size and shape requires knowing where one object ends, in our case, an IHC stained nucleus or cytoplasm, and the other begins.

Since an algorithm cannot be written to account for every possible variation, non-algorithmic computing is required.

The author was one of the first researchers to apply a combination of algorithmic and a non-algorithmic processing method known as an "artificial neural networks" to address the challenges of image processing of complex, three dimensional, cytological specimens.

Neural networks have been transforming artificial intelligence in biological systems and are well described by van Gerven and Bohte (2018). Briefly, instead of being programmed in advance with preset classification parameters, a neural network learns to perform a classification task by example. Mimicking the biological brain, hence the name, neural networks consist of electronic nodes which sum a signal received from numerous inputs generated by other electronic nodes.

These nodes are organized in a minimum of three layers. The input to the first layer is the digitized input from the environment (in our case a digitized image) and the output from the last layer is a score representing the classification. If the sum of the input

signals, each of which is multiplied by a "synaptic weight" is above a threshold, then the node "fires" and transmits its signal to other nodes.

An example of neural network training for cytology can be demonstrated from the classification between normal and dysplastic cells.

The cytological diagnosis of dysplasia is primarily morphologic and supported by molecular evidence. Among the key morphologic indicators of dysplasia are the increased nuclear to cytoplasmic ratio and the darker staining of the nuclear chromatin than in a normal cell.

Both of these morphologic appearances however, can be mimicked by two normal epithelial cells that partially overlap each other or by a normal cell being partially overlapped by a non- epithelial cell (RBC or inflammatory cell). Both of these artifactual "pseudo-dysplasias" outnumber actual dysplasia, as even in high grade dysplasia, the number of normal cells in the cytological specimen vastly outnumber the dysplastic cells. A typical ratio for a conventionally prepared abnormal cervical Pap smear is approximately 20 dysplastic cells scattered among 100,000 normal cells.

During training of the neural network, the input layer of the system is serially presented with the digitized images of a large set (in our case, over 1,000) of known paradigmatic normal and abnormal cells with numerous variations due to overlapping material. This is known as the neural network training set. Simultaneous with the presentation of each paradigm cell image to the input layer of the network, a desired

output score is presented to the output layer. This is typically .001 for a non-epithelial or IHC "negative" cell, and 0.999 for an epithelial or IHC "positive" cell.

At the initialization state (prior to training), the synaptic weights on all of the inputs to each of the summation nodes ("neurons") are small and random. That is, if a dysplastic image is presented to the input layer, the final score from the output layer will be random.

During network training, an error correction function to each of the synaptic multiplication weights of each of the summation nodes is "backpropagated" from the now known desired output, such that the next presentation of the same paradigmatic image will result in a score that is closer to the optimum .001 or .999 that the trainer knows corresponds to the input image.

After a number of iterations (usually about 200), the network demonstrates accurate classification of the training set, i.e. the digitized image of a dysplastic cell from the training set that is presented to the input layer will result in a high output score, and the digitized image of a normal cell will result in a relatively lower one. The outputs do not need to be 0.999 for a positive cell and 0.001 for a negative; just that the scores for the two sets being classified are sufficiently separated so that the desired classification accuracy with sufficient statistical significance is achieved.

At this point, training is stopped and the synaptic interconnection weights are fixed. In subsequent non-training ("feed forward") use, the network will be presented with new images that will result in output scores that reflect its prior classification

training. An illustration of the architecture of a multilayer neural network is shown in Figure 6.

In general, two uses can now be made of the output scores from feed-forward non-training use of the classification network. One is relative and does not contain a threshold, and the other is absolute and does contain a threshold.

To determine the presence of an absolute discriminant if an abnormal event is present on the specimen (i.e. does the patient have dysplasia or cancer?) a relative approach is typically used. Thus, high resolution images of a preset number of cells (typically 50-200) with the highest-ranking neural network output scores (i.e. the most abnormal appearing 50-200 cells selected by the network from the over 100,000 cells in the specimen) are presented to a trained cytologist or pathologist for review.
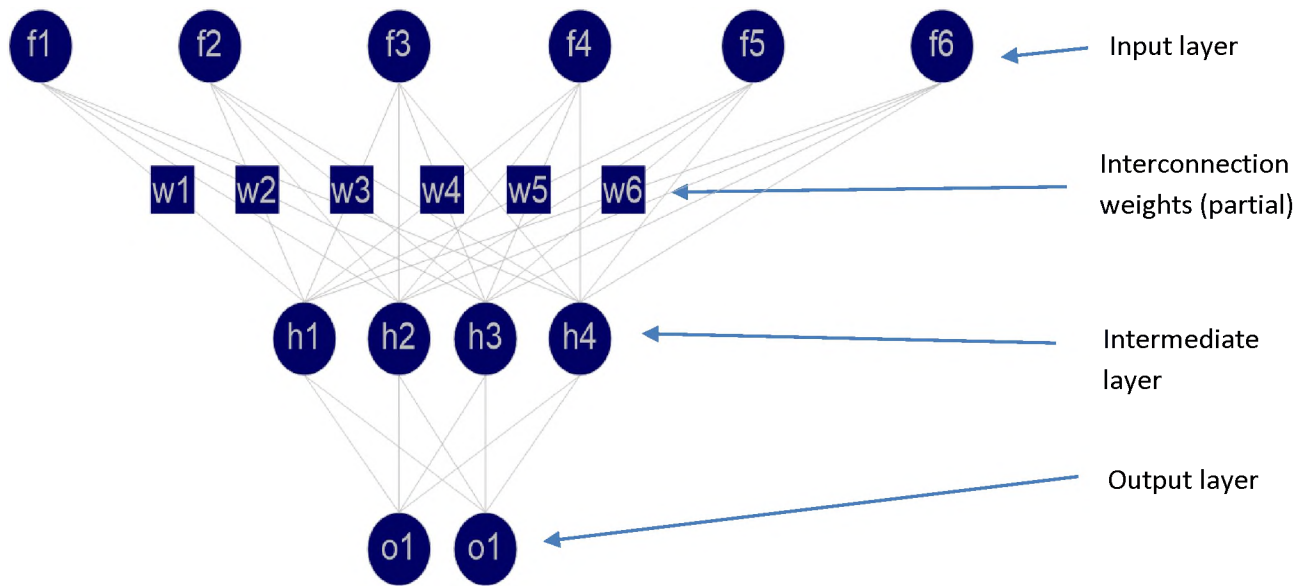
Figure 6. The architecture of an artificial neural network resembles that of biological neural learning systems. The input layer "neuron" (f1-f6) excitation levels are the result of digitization of the input signal to be classified. The output layer neurons (o1-o2) reflect the desired classification output during training and the feed forward actual classification post-training. Each of the interconnection "synaptic" weights (w) are multiplied by the signal from the preceding layer and are sent to the subsequent layer. If the sum of all of the signals following this multiplication that are received by a neuron at the next level is higher than a present threshold (usually 1) then that neuron "fires" with its "1" signal now being multiplied by the following layer of interconnection weights and are sent to the following layer. Prior to training the interconnection weights are small and random and are incrementally corrected during training to provide the desired classification result.

Unlike the sorting of the "most suspicious cells" used for the detection of dysplasia, for our application of quantifying the level of IHC, the inquiry is inherently relative, i.e. the question that is asked is if the IHC response on specimen A higher or lower than that of specimen B? As a result, an absolute numerical threshold approach can be used.

A threshold neural network output score is selected to represent a positive indication of antigenic presence of a true cell to the particular IHC stain, and the number of such positive cells provides the desired result.

The inherent accuracy of this neural network based quantitative IHC scoring system is demonstrated by positive signals (requisite stain intensity), which reflect antigenic response of true individual cells and not artifactual positivity that results from overlapping, relatively negative, normal cells and other material.

2.3.1 Detailed Description of the Quantitative IHC System Used in this Study

The primary classification step includes performing morphological filtering on an image of an IHC specimen to detect objects that have certain morphological features consistent with individual cells, such as a generally round shape or a certain size. The secondary classification step then further classifies these objects using an implementation of a neural network.

The primary classifier first performs an erosion of the image. This erosion operation successively peels off layers of pixels from each object in the image so that all

of the objects, which are smaller in size than the smallest known pathological cell nucleus, are removed from the image. The remaining objects are then dilated, i.e., regrown, by successively adding back layers of pixels to these objects, but they are not dilated to the point where they are touching each other. The basic operations of erosion and dilation are well described in the image processing literature (Serra).

The algorithmic component of the overall image processing system performs a primary classification of the image which finds the centroids of nuclei to be analyzed. Using a smaller sub-image centered around these centroids, the adaptive component of the overall image processing system performs a secondary classification which assigns each centroid a value indicative of the possibility that the object having that centroid is a cell of the type for which classification is being performed. Simultaneously, the centroids are also ranked based on the value assigned through the secondary, non-algorithmic (neural network) classification.

Secondary cell classification is performed by the neural network computer. The neural network utilizes the parallel structure of a two or three-layer backpropagation neural network emulated with pipelined serial processing techniques executed on one of a host of commercially available neural network computer accelerator boards.

The area of the slide found on a low magnification (50X) scan that possibly contains the biological matter on the specimen is segmented into a plurality of rows and columns, for example, 20 rows and 50 columns of equal sized blocks. Each block occupies

an area of the slide, for example, approximately 2000 microns×1600 microns, and corresponds to an individual image to be viewed at one time by the microscope.

Each block is subdivided into sixteen equally sized analysis fields. Each field is thus, approximately 500 microns by 400 microns in size. Once digitized by the image processor, each analysis field will be represented by a 256 by 242 matrix or array of pixels which corresponds to a resolution of approximately two microns per pixel during a low resolution scan or high resolution scan, or a 512 by 484 array of pixels corresponding to a one micron per pixel resolution during a high resolution rescan.

Each pixel then represents the brightness or gray scale density of a discrete area of the analysis field image. The gray scale density of each pixel is further represented by an 8 bit digital value. Consequently, each pixel will represent an area of the analysis field image 62 by a gray scale level ranging from zero to 255.

The computer performs a low resolution scan on each analysis field of the microscope slide to determine if that field contains biological matter, and a high resolution scan on each of the analysis fields having biological matter to detect objects contained therein which are likely to be epithelial (i.e. neither debris, inflammatory cells, or red blood cells.)

During the low-resolution scan, the objective of the microscope is set at its 50X magnification power and the microscope begins scanning the individual blocks of the slide. For each block, the microscope also automatically determines the approximate focal plane for that area of the slide. This is necessary since the cover slip covering the

specimen can be somewhat wavy or possibly angled, due to air bubbles contained under the cover slip; the resultant focal plane may thus vary from block to block.

Once the focus is determined for the block being viewed, the camera captures the image of the block and sends that image to the image processor through the digitizer. The image processor then subdivides the block into analysis fields and determines whether there are areas of interest in each analysis field corresponding to objects which may be biological material. If a field contains material which may be biological, the block is identified along with its approximate focal plane and stored in memory for future analysis during the high resolution, 2 micron/pixel scan.

Initially, a scan path is determined which will allow the microscope to view each block possibly containing biological matter with the least amount of movement of the slide. For the high-resolution scan, the 10X objective is inserted into the viewing path of the automated microscope and the scan is begun at the first block in the scan path.

The camera first acquires a stack of z-images which are sent to the image processor to synthesize the composite in-focus EDF image, as described below. The image processor then performs the primary classification of the objects in each analysis field as discussed more fully below. This primary classification finds the centroids of nuclei in each field that have the correct size and gray scale density characteristics of an epithelial cell. (Figure 7)

When an object in an analysis field has been identified as having the size and gray scale density characteristics of an epithelial cell, a 24×24 array of pixels surrounding the

object centroid, called a net image, is transferred to the secondary neural network classifier for further classification and IHC stain intensity scoring. A net image is approximately 48×48 microns in size at a resolution of 2 microns per pixel. As an epithelial cell nucleus tends to range between 10 and 40 microns in diameter, the net image is sufficiently large to contain a complete image of a cell.

The primary algorithmic classifier performs a morphological "well" or "bottom-hat" algorithm which filters out objects that are the size of an epithelial cell or smaller. (A "well" algorithm is the inverse of a morphological "top hat" algorithm.) The resulting image, containing only objects which are too large to be a cancerous cell nucleus, is then subtracted from the original image containing all of the objects. Consequently, what are left are objects of the correct size or smaller.

A separate image is then prepared from the original image, which contains only those objects which are too small to be epithelial cells, but likely represent inflammatory or red blood cells. When this latter image, containing only objects which are too small to be epithelial cells, is then subtracted from the image having objects of the size of an epithelial cell or smaller, the resultant image will thus contain only images being of the size of an epithelial cell.

The centroids of the objects in this image are then determined and the images centered around those centroids are sent to the secondary neural network classifier for further classification.
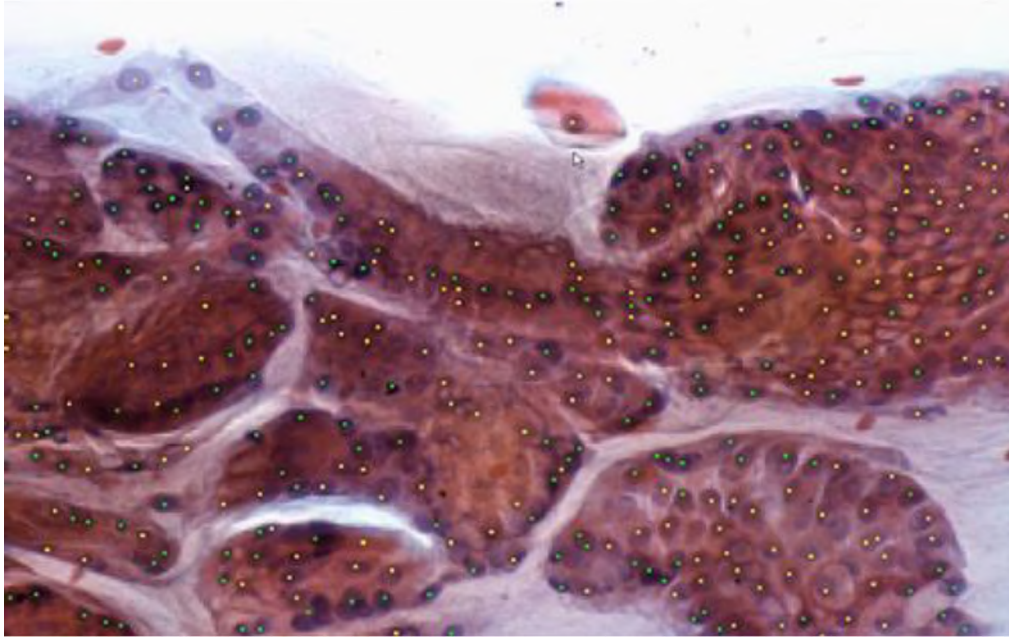
Figure 7. **The primary algorithmic classifier finds the centroids of nuclei in each microscopic field.** The primary algorithmic classifier is programed to identify the centroids of nuclei in each microscopic field of view that have the correct size and gray scale density characteristics of an epithelial cell. These are shown as the yellow and green dots.

Steps of the Primary Classifier "well" algorithm:

The image in the frame buffer, which corresponds to an analysis field and is referred to herein as the frame image, is spatially filtered such with a Gaussian low pass filter to remove random noise from the image. The Gaussian filter has a convolution mask of:

```
1 2 1

2 4 2

1 2 1
```

This convolution mask is moved across every pixel in the frame image.

To clarify, the convolution mask will be initially centered on the first pixel in the frame image pixel matrix. Consequently, the 8-bit gray value of this pixel will be multiplied by 4 while the 8-bit gray values of the pixels immediately above and below and on either side will be multiplied by 2, and the adjacent diagonal pixels will have their 8-bit gray scale values multiplied by 1. All nine of these results are summed and the result is divided by 16 and placed in a pixel location in a result frame corresponding to the location of the center pixel. The convolution mask is then shifted to the next pixel in the frame image pixel matrix and the operation is repeated. This continues for all pixels in the matrix, thus generating a complete result frame.

A morphological "closing" operation is then performed to filter out all dark objects smaller than an epithelial cell nucleus. This morphological closing is performed using a

series of gray scale "dilation" operations followed by a series of gray scale "erosion" operations.

Gray scale "dilation" is a mathematical morphology term used in image processing to denote an operation wherein a pixel is replaced by the maximum value of its neighboring pixels and itself.

Erosion is a similar term wherein the center pixel is replaced by the minimum value of its neighboring pixels and itself.

Gray scale dilation is performed first using a square neighborhood consisting of the eight horizontal, vertical and diagonal neighbor pixels. This is followed by a second dilation with a diamond neighborhood consisting of the four horizontal and vertical neighbor pixels only.

For the erosion operations, a gray scale erosion operation is first performed using a diamond neighborhood, followed by an erosion using a square neighborhood.

The combination of operations using these masks morphologically approximates an octagon, which is digitally analogous to the morphology of an epithelial cell or cell nucleus which tends to be generally round.

The manner in which this morphological closing filters small objects out of the image is graphically represented in Figure 8. The figure illustrates two objects; the object on the right is a large dark nucleus and the objects on the left are smaller, less dark inflammatory cells and debris. The horizontal line represents a row of pixels passing

through the objects. The gray scale values for this row of pixels are superimposed. The

large dark nucleus forms a wide and deep gray scale rectangle due to its relatively large

size and darkness. Inflammatory cells and debris, relatively smaller and less dark, form a

narrower, shallower trough.

(a) Initial image = 0.7x
(red + green components)

(b) Gaussian smoothed image

(c) Dilation by 8-neighbor square

(d) Dilation by 4-neighbor diamond

(e) Erosion by 4-neighbor diamond

(f) Erosion by 8-neighbor square
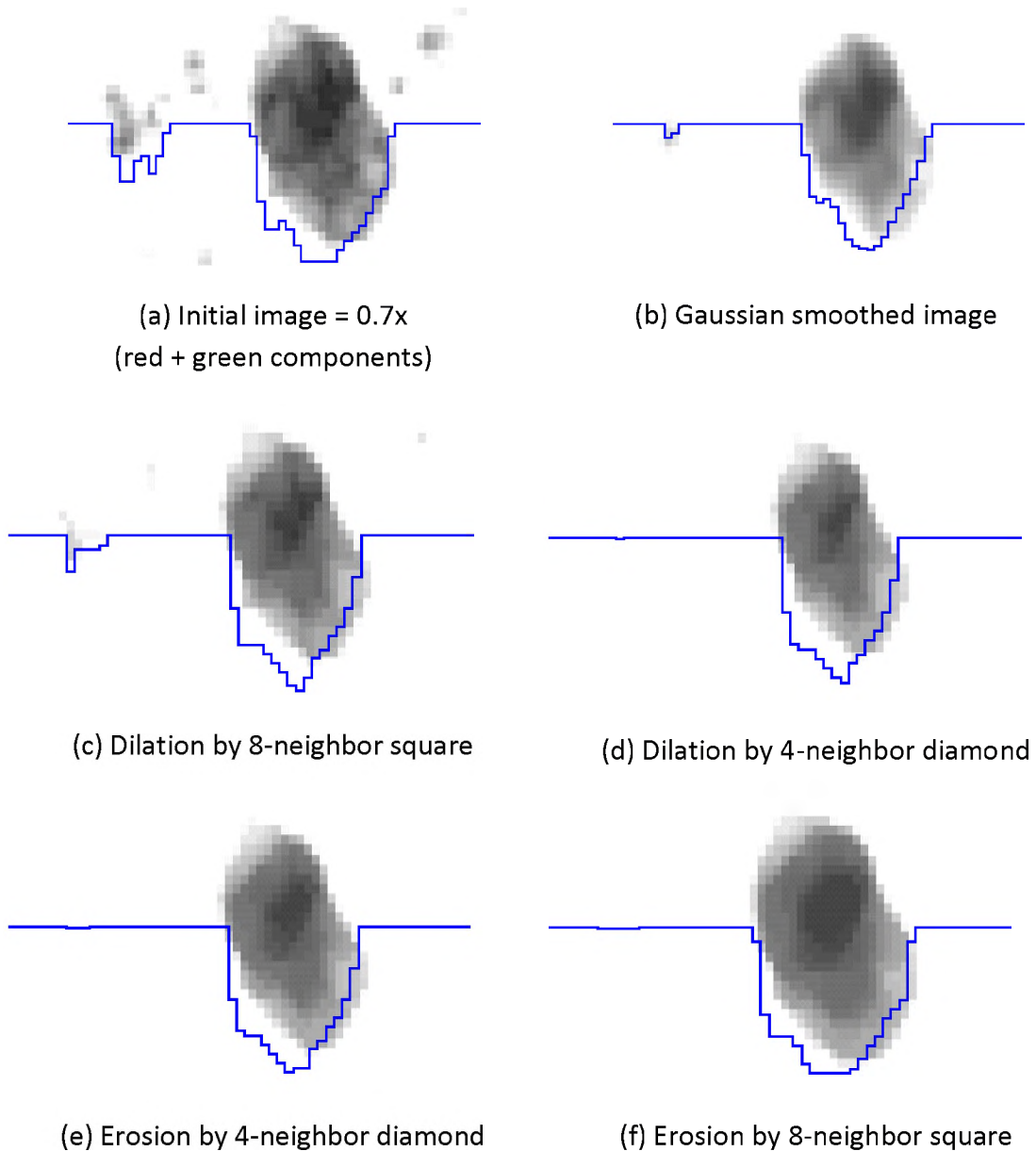
Figure 8. Morphological closing operations are used during primary algorithmic classification to prepare the cellular image for secondary neural network classification. Morphological closing operations are used during primary algorithmic classification to smooth and center the cellular image in preparation for secondary neural network classification. Plot of pixel values on horizontal line across image showing initial gray scale image (a), and a sequence of dilations and erosion (b) through (e), resulting in the morphological closing image (f).

As dilation operations are performed, these gray scale troughs are gradually filled. After one such dilation operation (step {c}), the large dark nucleus may now be represented by the relatively wide depression while the inflammation/debris may be represented by the narrow trough. Subsequent dilation operations will continue to fill in these depressions. Consequently, a relatively small object will be completely filled in while larger, darker objects, such as malignant nuclei, will remain as somewhat narrower depressions.

When the image is then subjected to a series of erosion operations, the narrow depressions which are the gray scale representations of large, dark objects will be expanded to approximately their original size and shape, whereas the completely filled in gray scale representations of small objects will not be eroded. The morphological closing will thus yield an image in which objects significantly smaller than malignant or premalignant nuclei are filtered out.

This dilated eroded frame image is then subtracted from the frame image which has been Gaussian filtered but not dilated and eroded (step {b}, Figure 8). The resultant image thus consists only of objects which generally smaller than the size of an epithelial nucleus.

A threshold operation is then performed on this image with pixels having a gray scale value above a certain threshold being assigned a binary `1`, and those pixels have gray scale values below that threshold being assigned a binary zero. The threshold is chosen to filter out objects which are not dark enough to be cell nuclei. A binary 3×3

erosion is then performed on the image to remove the outer pixel boundary of the remaining objects, thus making the objects narrower by one pixel in all directions. This binary erosion is accomplished by performing a Boolean AND on the center pixel and the eight neighboring pixels.

The frame image now contains objects of the appropriate gray scale density that are smaller than epithelial cells of interest. These smaller objects typically represent white and red blood cells and debris. Consequently, these objects must be removed from the frame image. Since the frame image is now in a binary format, a binary mask is needed to mask off the smaller objects. Accordingly, the mask would have binary `1`'s in all locations of the frame image pixel array except for those locations occupied by a small image, where there would be zeros. Consequently, by Boolean ANDing the binary frame image with the binary mask the small objects are removed and predominantly what is left are objects of the appropriate gray scale density and size for an epithelial cancer cell nucleus.

This mask is obtained by taking the untreated frame image stored earlier and treating the image with a Sobel operator to find areas within the image having relatively large arithmetic gradients. Areas of high detail in the image, or areas having relatively small objects, will have large gradients. The Sobel operator, which is essentially a high-pass image filter, will pass those areas having large gradients and reject the areas of large objects which have smaller gradients. By choosing the correct filter parameters, the edges of objects are found. The image is then thresholded to convert the gray scale image into a binary image. A 3×3 binary dilation is then performed on the image to slightly expand

or thicken the edges in the image. The binary dilation operation is performed as a Boolean `OR` operation.

The dilation operation is then repeated using only the adjacent pixels. After this edge thickening operation, objects smaller than a certain diameter will have become solid "blobs" and objects larger than this diameter will remain open in the center. This function could also be performed with a gray-scale morphological well or top hat filter as described above with its parameters set to find smaller objects.

A number of the outermost rows and columns of pixels, for example, eight, forming a border around the frame are then removed, as they contain artifacts and other irrelevant information introduced by the operations performed above. The complement of the resultant image is then taken by a Boolean `NOT` operation. Consequently, the binary image will consist of binary `1`'s in all locations except in the slightly enlarged areas encompassing objects too small to be epithelial cells. This complemented image thus forms the binary mask used to subtract the small objects from the earlier developed frame image. When Boolean ANDed with the frame image having objects of the appropriate size and smaller, the small objects are eliminated.

Once the small objects have been removed and the frame image contains predominantly objects having a gray scale density and size compatible with the gray scale density and size of an epithelial cell nucleus an operation is performed to suppress isolated white pixels in the frame image. These isolated white pixels (binary `1`) constitute

noise introduced during any of the previous operations and are not of a sufficient size to be a cell nucleus.

Once these isolated pixels have been suppressed, a "shrinking" operation is performed four times). "Shrinking" is a Boolean operation commonly used in image processing. The shrinking operation successively removes layers of pixels around the object in the image frame until, for an object of the appropriate size, only one pixel or no pixels remain. In the case where the object is completely removed, the last pixel removed is replaced with a binary 1. Since the outer layers of pixels of the objects were successively removed progressing inwardly, the remaining or replaced pixel will represent the approximate center or centroid of the object. Any objects remaining in the image which are larger than one pixel are removed, as they correspond to something which is larger than an epithelial cell nucleus would be.

A 24×24 array of pixels surrounding each centroid, (the "net image", identified by the primary classification function of the image processor is then transferred to the general processor for storage. A secondary classification of the objects represented by these net images is then performed.

2.3.2 Secondary Non-Algorithmic Classification

The algorithmic processor described above individually transfers each net image to the neural network for secondary classification. The task of the secondary classification

is to distinguish true epithelial cells from other objects of the same size which may pass the primary algorithmic classifier, such as cell clumps, debris, clumps of leukocytes and mucus.

Based on training performed with a training set of 500 true and false epithelial cell images, as described more fully above, the neural network assigns each net image with a value, called a net value, ranging from 0.001 to 0.999, as determined by the likelihood that the object is an epithelial cell. This score in then multiplied by the integrated optical density (IOD) score of the IHC stain intensity in that net image. Integrated Optical Density is a summation of the total of the grey sale values of each pixel in the image. Thus, a smaller cell that is strongly responsive to the IHC stain and a larger cell which is less heavily stained can both represent the same total amount of antigenic response.

Consistency of neural network results is enabled by the fact that each net image presented to the secondary classifier is pre-centered through the algorithmic primary classification on the centroid of the epithelial cell nucleus, as described above.

In many previous attempts to utilize neural networks and other high-level template matching pattern classifiers for image recognition, difficulty has been encountered in consistently presenting the neural network classifier with the centroid of the image requiring classification.

To use an example from another application domain, back propagation neural networks are excellent at reading handwritten zip code digits but have difficulty in finding

where the zip code is on the envelope. This system for cytological IHC scoring overcomes this difficulty through its robust algorithmic classification.

Proper generalization during actual classification operation is enabled by the fact that the secondary adaptive classifier is presented with precisely the same type of neural network images on which it was trained. The images processed by the system are also centered on the centroid of the suspect nucleus by the primary classifier in a manner identical to that used to prepare the training set images.

As noted above the secondary neural network classifier was trained to associate a known non-epithelial image with an output of 0.001 and a known epithelial image with an output of 0.999. Such outputs represent the degree of certainty that an image is an epithelial cell not.

When the secondary classifier is presented with new, unknown images, it generalizes from its training and attaches a net value to the image. The closer that the secondary classifier is able to categorize the unknown image into the non-epithelial cell category, the closer is its net value equal to .001.

Conversely, the more closely that the unknown image appears to resemble the true epithelial cell images of its training set, the closer is the net value assigned to that image equal to 0.999

On each tissue cut of a transepithelial brush biopsy prepared for IHC approximately 50,000 individual cells may be present. Of those approximately 2,000 will

consist of touching or overlapping normal cells that will produce an artifactual positive IHC signal due to low levels of normal stain intensity combining and appearing as a single positively stained cell. On a truly positive specimen there may be 100 individual positively staining cells. The task of the overall system is to: 1) differentiate between these potential 100 truly positive cells and the 2,000 false positive signals caused by cellular overlap or other artifacts and then 2) produce a neural net output score that is a composite of the neural network score of an algorithmically selected centroid image as most closely resembling an epithelial cell, and the Integrated Optical Density of the IHC intensity of that centroid.

In this example the image processing system operates by having the digitized images of all 50,000 cells on the specimen examined by an algorithmic classifier prior to employment of the neural network.

The function of the algorithmic classifier is to identify the potentially abnormal images which will require subsequent analysis by the neural network. Use of the algorithmic classifier accomplishes two goals. It sharply reduces the number of objects which will need to be examined by the neural network (in this example 48,000 of the 50,000 objects on the specimen will not require neural network analysis) and it also finds the centroids of each object sent to the neural network which sharply decreases subsequent processing variability (i.e. all images sent to the neural network for scoring are pre-centered).

Integrated Optical Density (IOD) is a particularly useful measure in IHC stain intensity determination as it automatically integrates stain intensity (the grey scale score of each pixel) and the size of the area that is demonstrating an antigenic reaction.

The final neural network score is thus a sum of the IOD score and the morphological finding that the stained image is a true epithelial cell.

2.4 Computer synthesis of the *enface* view of glandular tissue as an independent measure of dysplastic atypia on transepithelial cytological specimens from Barrett's Esophagus

To verify the accuracy of our proposed method for differentiating between dysplastic and inflammatory atypia, an independent "gold standard" for the presence of dysplasia is required. For the presence of dysplasia in Barrett's esophagus, this independent gold standard is provided by a computer synthesized *enface* view of the suspect dysplastic gland.

Barrett's esophagus, an acquired condition that occurs as a result of chronic, recurrent acid-induced damage to the internal lining of the esophagus and first described in the 1950's, is technically referred to as intestinal metaplasia.

The normal esophagus is lined with a squamous epithelium. It is believed that in response to chronic acid reflux, the epithelial stem cells in the basal layer of the esophageal epithelium differentiate into a columnar epithelium that resembles the

normal epithelium of the small intestine (Spechler and Souza 2014). While not dysplastic in itself (i.e. it is not believed that the metaplastic epithelium contains genetic mutations), this area of intestine abnormally located in the esophagus is a neoplasm and is over twenty times more likely to become cancerous than normal squamous epithelium (Shaheen and Ransohoff 2002).

As a patch of intestine, the Barrett's epithelium contains the adaptations which have evolved to optimize absorption of nutrients. Only in very modern times has obesity and weight loss become a public health concern worldwide however, for much of the world today, the current challenge is still to obtain enough nutrients from each meal so that we could survive until the next.

Optimization of nutrients occurs on three levels. First, the small intestine is over 20 feet long providing a great deal of surface area through which food passes to extract glucose and other nutrients.

Secondly, the surface of the twenty-foot-long intestinal epithelium is organized as individual villi, vastly multiplying the surface area for absorption. Thirdly, the columnar cells that line each of these villi and actually perform the transfer of nutrients from the intestinal lumen into the blood vessels that lie in the center of each of the villi are packed as tightly as possible.

The most efficient way to pack any cylindrical object is as a honeycomb. It is for this reason that non-dysplastic absorptive glandular epithelium is organized as a

honeycomb when viewed from perspective of the surface of the gland, i.e. the *enface* view.

One of the earliest morphologic indications of dysplasia is effacement of this typical honeycomb pattern. This is because development of carcinoma is characterized by de-differentiation, i.e. the constituent cells begin a process of acting independently and no longer appear as if they are a component of their originating tissue.

When a forceps biopsy specimen is obtained of any tissue, including a forceps biopsy specimen of intestinal metaplasia, it is universally embedded in paraffin and is then sliced by the microtome into 3-4 micron sections. This is done because the depth of field of a standard manual microscope is limited to 3-4 microns.

Slicing of the gland almost always destroys the *enface* view as is illustrated in Figure 9. In order to preserve the *enface* view of the gland, a three dimensional microscopy system can be utilized which allows examination of tissue specimens up to 150 microns in thickness. The Extended Depth of Field (EDF) system detailed below system operates by taking up to 50, 3-micron views of the tissue along the z axis. Somewhat similar to a CAT scan, each of these two-dimensional images is then integrated together to provide a three-dimensional image of the tissue which preserves the *enface* view of the gland.
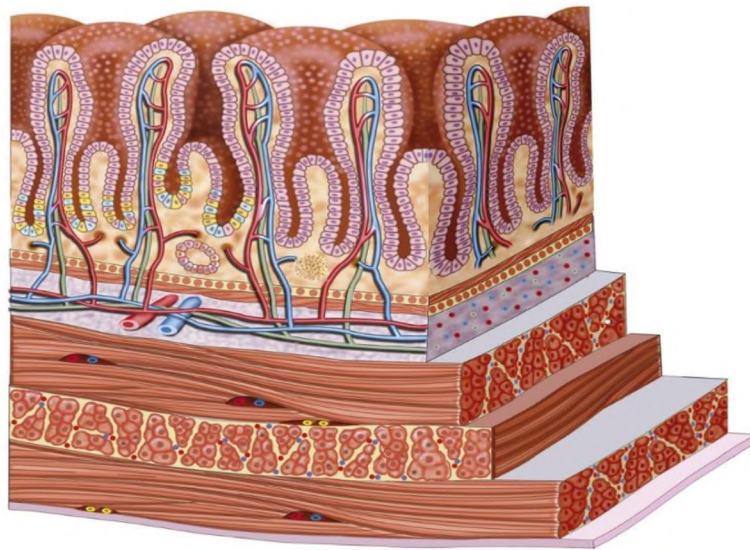
Figure 9. Normal slicing of the intestinal gland almost always destroys the *enface* **view.** The cellular orientation of the outside surface appearance of the gland (shown as white dots here) is typically not visible on the thin tissue sections that result when the gland is sliced by the microtome.

2.4.1 Extended Depth of Field Microscopy

High-resolution microscopy suffers from limited depth of field, which prevents thick or uneven specimen preparations from being imaged entirely in focus. Objects that appear outside the narrow depth of field or focal plane become quickly blurred and out of focus (Figure 10).
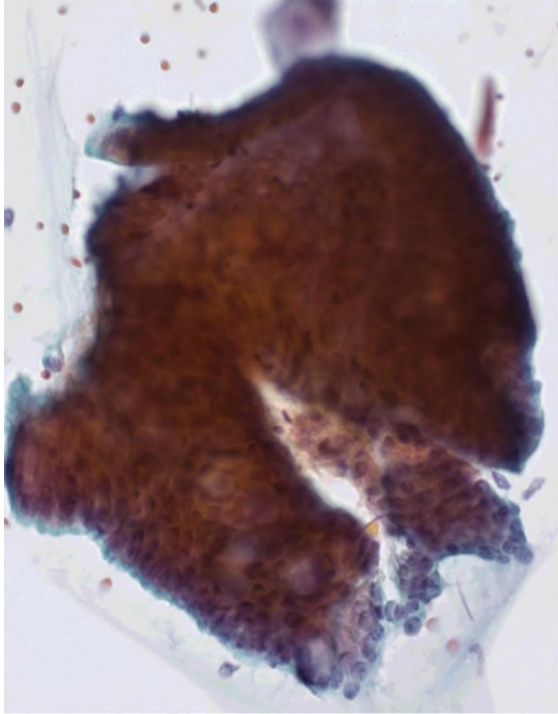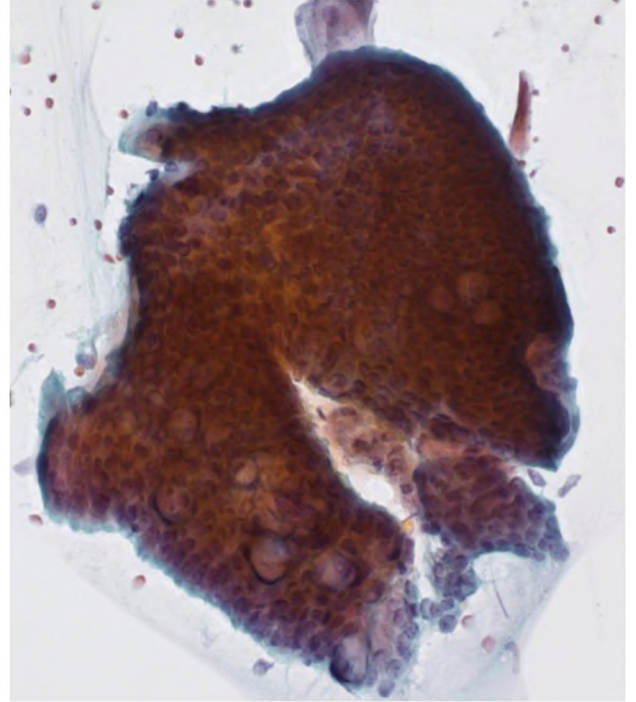
(a)   (b)

Figure 10. **Extended Depth of Field (EDF) Microscopy allows the entirety of a highly thick tissue specimen to be in focus.** In conventional microscopy much of this thick tissue specimen appears indistinct and out of focus even at its best focal plane (a), but is sharp in the EDF image (b).
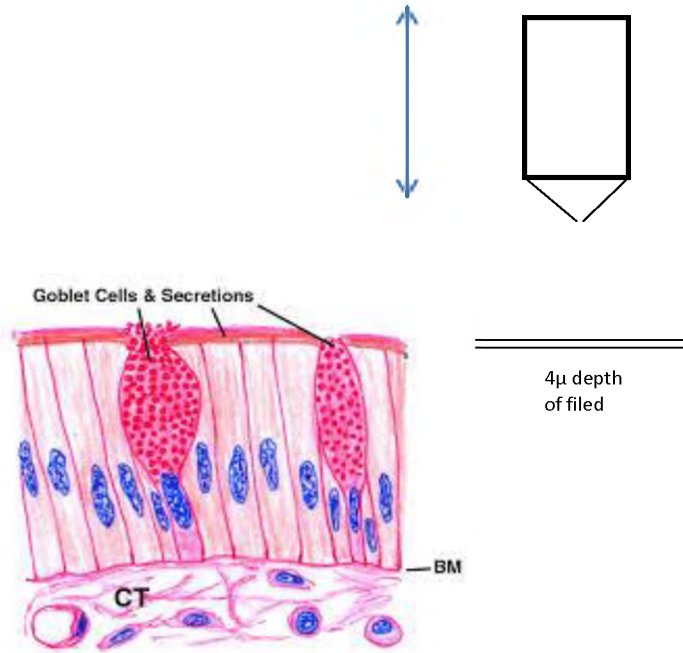
Figure 11. Standard microscopy that is limited to a 3-4μ depth of field cannot capture the *in vivo* appearance of a 500μ thick epithelium. A standard microscope with a 3-4μ depth of field cannot be practically utilized to focus on an up to 150μ complex mucosal tissue sample deposited on the slide that derived from a 500μ thick transepithelial sample consisting of columnar cells (E) and goblet cells (GC) on top of basement membrane (BM), lamina propria/connective tissue (LP/CT).

Moreover, this limited depth of field becomes worse as the magnification increases because it is directly dependent on the numerical aperture of the microscope objective, which increases with the magnification.

Thick tissues that are thicker than the depth of field of a microscope objective introduces a third dimension to a biopsy sample, in effect, making the specimen or portions thereof, three-dimensional in space. As a consequence of the three-dimensional character of a specimen, the cellular material is located at various focal planes, which thereby requires constant focusing and refocusing to observe cells at various contours of the sample.

Specifically, when obtaining a transepithelial non-lacerational brush biopsy of a tissue, a cytology brush is used, which is sufficiently stiff so that it penetrates all of the layers of epithelium. In the process of obtaining a full thickness tissue specimen, tissue fragments, in addition to single cells and cell clusters, are obtained and transferred onto a microscope slide. These specimens are markedly different from the cell monolayers prepared for the analysis of exfoliative cytological specimens, whereby only a superficial sweep of a tissue is conducted, and no tissue fragments are obtained.

The transepithelial cytology specimen, containing single cells, cell clusters and tissue fragments, is essentially a hybrid between a cytological smear and histological sections. The ability to view tissue fragments, in addition to single cells, confers a decisive informational advantage for pathologists to distinguish inflammatory atypia from dysplastic atypia.

Diagnosis of dysplasia is typically based on a combination of tissue and cellular morphology. As in all epithelial tissues, the morphologic impression of the degree of dysplasia (Mild Grade Dysplasia, Moderate Dysplasia, Severe Dysplasia, and Carcinoma in Situ/Cancer in the squamous epithelium and Low-Grade Dysplasia (LGD), High Grade Dysplasia (HGD), and Carcinoma in Situ/Cancer in the glandular epithelium) is assumed to be associated with an increasing number of functional genetic errors. In the abnormal glandular tissue of the esophagus (Barrett's esophagus), LGD has been found to be typically associated with 3-5 functional genetic errors, HGD with 5-7 errors and CIS/Cancer with 8 or more functional genetic errors. (Personal communication from Matthew D. Stachler, Harvard Medical School, of data currently in preparation)

(a) Non-Goblet Cell Intestinal Metaplasia

(b) Barrett's Esophagus (Goblet Cell Metaplasia)

Goblet cells

(c) Barrett's Esophagus with Low Grade Dysplasia

(d) Barrett's Esophagus with Inflammatory atypia

(e) Barrett's Esophagus with High Grade Dysplasia
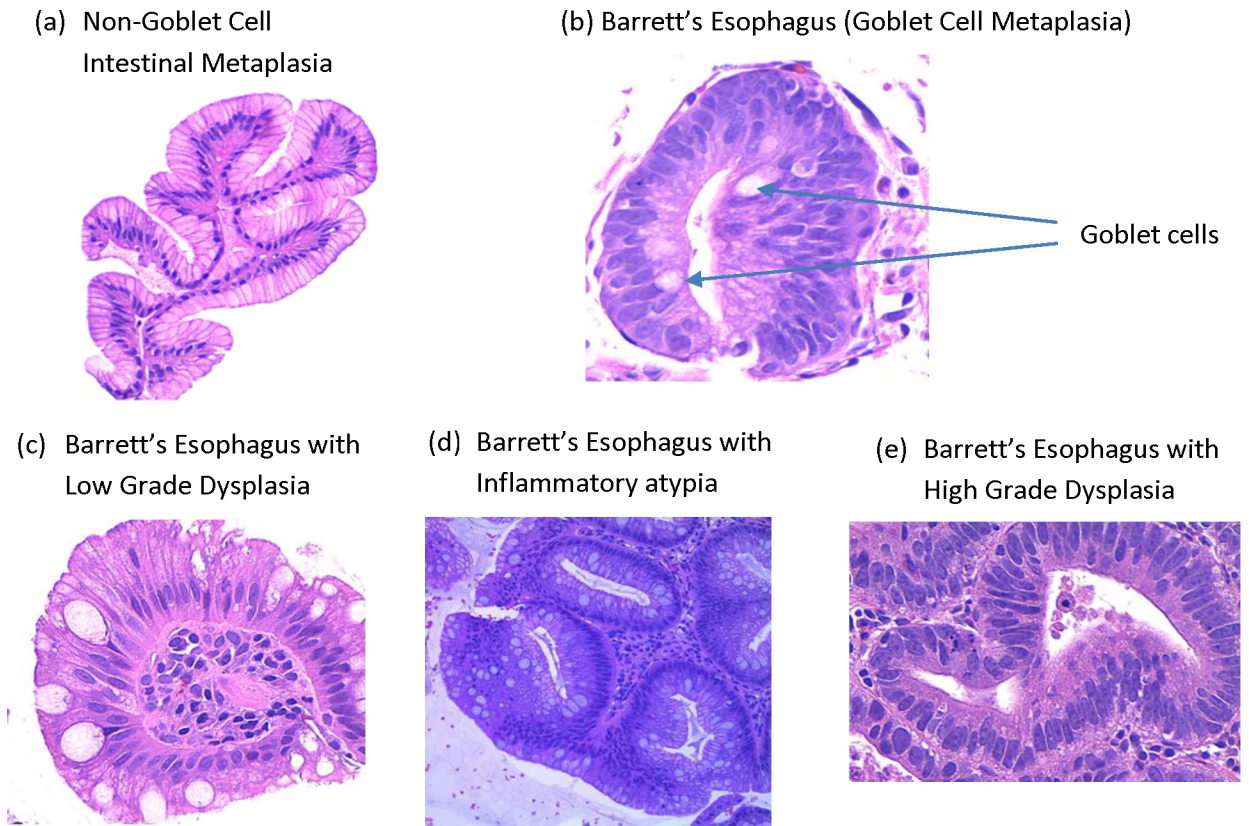
Figure 12. Barrett's Esophagus with Inflammatory Atypia and Barrett's Esophagus with Low Grade Dysplastic Atypia are often morphologically Identical. Shown are examples of (a) Non-goblet cell intestinal metaplasia; (b) Barrett's esophagus without dysplasia; (c) Barrett's esophagus with Low Grade Dysplasia; (e) Barrett's esophagus with High Grade Dysplasia, and (d) a case of Barrett's esophagus with indefinite atypia that was assumed to be inflammatory demonstrating its morphologic resemblance to the Barrett's esophagus with Low Grade Dysplasia shown in (c), and Barrett's esophagus with High Grade Dysplasia (e) – Transepithelial brush biopsies of intestinal metaplasia of the esophagus Glandular esophagus, H&E,) Transepithelial cytology specimens of Barrett's Esophagus were centrifuged into a pellet which was paraffin embedded, sliced, and stained with the H&E 100X (a), (c), (d) 400X (b), (e)

The diagnosis of HGD is based upon the degree of morphologic cytologic atypia alone. Architectural change is not required. By contrast, the diagnosis of LGD is challenging because the lower degree of morphologic atypia associated with LGD can appear identical to morphologic atypia that occurs in the presence of inflammation. (Figure 12). As such, a heuristic is used. If the cellular atypia extends from the bottom of the crypt to the top of the gland (lack of surface maturation), then the diagnosis of Low Grade Dysplasia is used; however, if it does not, "Indefinite for Dysplasia" will be diagnosed.

As noted above, if the three dimensional view of the intact gland is preserved by EDF microscopy, then the *enface* view is also preserved and this provides a definitive discriminant between inflammatory and dysplastic atypia, i.e. dysplastic effacement of the normal "honeycomb" pattern of the gland is not caused by inflammation and is thus, an early and reliable sign of true dysplasia.

With EDF processing, an automated microscope captures a set of 2D images taken at different focal planes at the same location on a slide and then combines these images to form a single 3D composite image. A single high-resolution image cannot be in-focus everywhere. With EDF processing, an automated microscope captures a set of images taken at regular z-intervals at the same location and then recovers from each slice those pixels that are in focus to build a single composite image from the in-focus pixels. Once the in-focus pixels of each image are fused into one image, the resultant image is essentially in-focus everywhere.
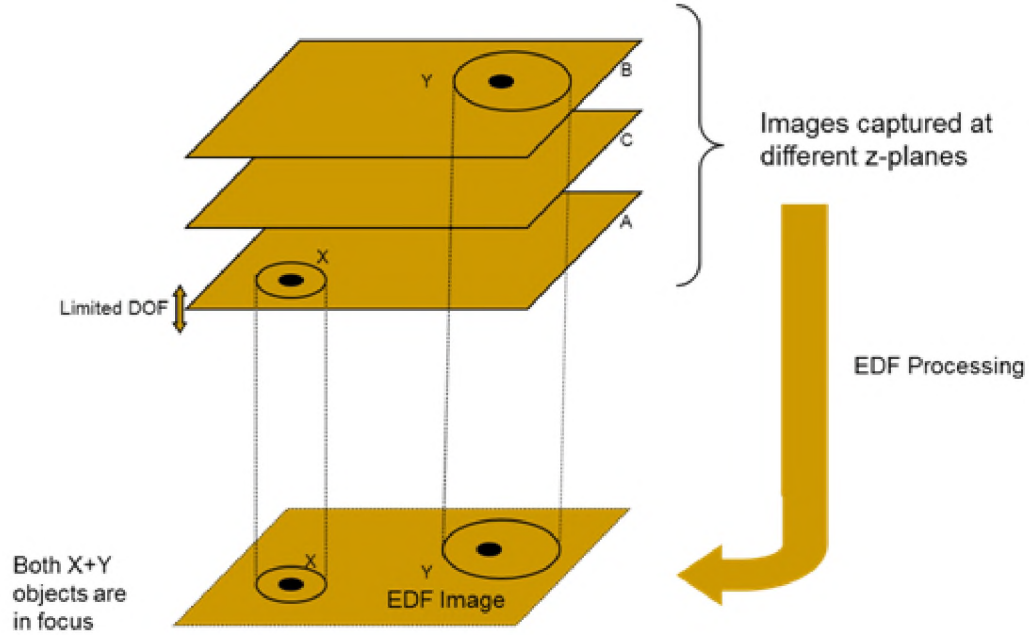
Figure 13. An extended depth of field (EDF) algorithm synthesizes up to 50 separate two dimensional focal planes to form a single three-dimensional image. To analyze the thick transepithelial cytology image, an extended depth of field (EDF) algorithm synthesizes up to 50 separate 3μ thick two-dimensional focal planes to form a single three-dimensional image. An automated microscope captures a set of images taken at regular z-intervals at the same location and then recovers from each slice those pixels that are in focus to build a single composite image from the in-focus pixels. Once fused into one image, the resultant image is essentially in-focus everywhere.

Standard EDF algorithms, which are ideal for creating a composite image of the top surface of a three-dimensional opaque object (Figure 14) do not work well for biological specimens, which present an additional complexity of having multiple semi-transparent objects or cells stacked on each other.

| (a) | (b) | (c) |

Figure 14. Standard EDF algorithms are designed for application to opaque objects. Lower half of image in focus (a) is combined with upper half (b) to create a composite image (c) in focus throughout. This works well for substantially opaque objects like the image of the housefly here.

The failure of standard EDF to properly process semi-transparent biological images results from the fact that in composing a composite image, standard EDF algorithms blindly extract the sharpest pixels from each focal plane, raising the possibility that a composite cell image contains pixels originating from multiple cells that happened to be situated on top of each other in the z axis. In that instance, a composite image may appear to represent a single cell, when in fact there were several cells stacked on top of each other, each of which could be observed by a microscope due to their semi-transparent character. When attempting to construct a composite 3D image of a semi-transparent biological sample for diagnostic purposes, it is critical to have all the pixels come from a single object or cell to avoid pixel contamination.

In order for an EDF algorithm to be properly applied to thick, semi-transparent biological specimens, it must take into account which pixels belong to which object and preserve most of the pixels of that cell or object, even though they may not necessarily be sharp (Figure 15).
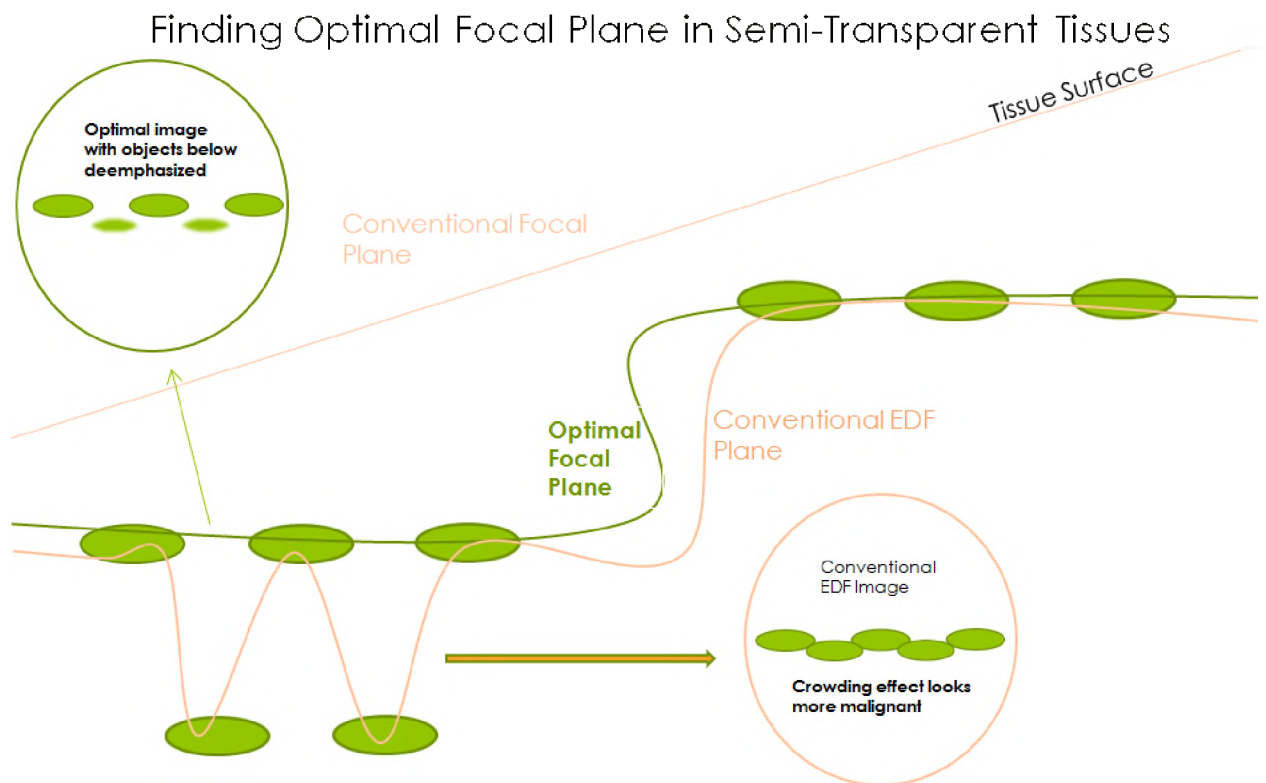
Figure 15. Standard EDF algorithm's that are designed for the analysis of opaque images require modification for use with semi-transparent biological material. An extended Depth of Field (EDF) algorithm for semi-transparent tissue will find the optimal focal surface (green), while standard EDF finds the noisy surface (pink), resulting in nuclear crowding artifact.

In summary, the semi-transparent quality of biological specimens presents a problem with applying standard EDF algorithms to thick cellular specimens. These standard EDF algorithms were designed to create a composite image of the outside surface of an opaque three-dimensional object. By contrast, with biological specimens, the area of interest is not limited to the outside surface, but rather there are areas of interest below the outside surface of a specimen.

Due to light absorption within a tissue, structures on the surface have a tendency to have a higher contrast or sharpness than structures inside a transparent tissue. Because tissue is comprised of a mass of cells, a pathologist needs to see the cells and nuclei that are situated below the outside surface, which comprise the thickness of the tissue. Additionally, due to the disaggregated nature of the cellular samples obtained by a transepithelial brush cytology instrument, a slide prepared in connection with such a specimen will inevitably contain cells that overlap and overlay each other. Consequently, an examining pathologist or specialized computer would want to build a constraint into the EDF algorithm such that pixels of objects can come from one object or cell only and not from neighboring objects that are situated either on top or beneath the cell being imaged. For the purpose of this document, this requirement is referred to as "PCO" or Pixel Constrained to an Object". Furthermore, there are objects of no diagnostic significance, such as cell walls or artifacts that should be deemphasized or eliminated from a composite image. To meet the PCO requirement, a morphological closing is applied. A closing is a dilation followed by erosion, to close any small holes in the nuclei and goblet cells, in effect assuring that pixels come from the same object.

A stack of successive images was acquired using the microscope. The focal distance between two slices is equal to half of the depth of field for the microscope objective used to meet the Nyquist criteria of optimum sampling.

An erosion algorithm was used to strip away a layer or layers of pixels from both the inside and the outside surfaces of an image.

The software then optimizes the number of z-slices processed, adapting the number of slices to the depth of the sample. During motion of the z-stage, the software detects when all pixels of the image are out-of-focus, or have past the slice of maximum sharpness. In this case, it is not necessary to take any more z-slices, thereby speeding up the processing.

Once all the areas of interest on a slide have been processed by the system, it is configured to stitch together the stored composite images in order to build a three-dimensional digital image of the entire specimen- or of areas of interest from it.

After assembling the various composite slices, the resulting digital image of the specimen is in-focus substantially everywhere and comprises only diagnostically important cellular features. Most importantly, the *enface* view of the glandular surface, a perspective that is normally destroyed by standard microtome sectioning, is maintained, allowing for an architectural diagnosis of dysplasia when the normal honeycomb pattern is disrupted.

An example of a dysplastic and non-dysplastic gland on the same tissue sample is shown on the computer synthesized image in Figure 16. As demonstrated in the image, the normal honeycomb pattern characteristic of the *enface* view of the surface of Non-Dysplastic Barrett's Esophagus (NDBE) has been effaced in the dysplastic gland directly above it.

(a) Dysplasia – Honeycomb Pattern Disrupted

(b) Non-Dysplastic– Normal Honeycomb Maintained

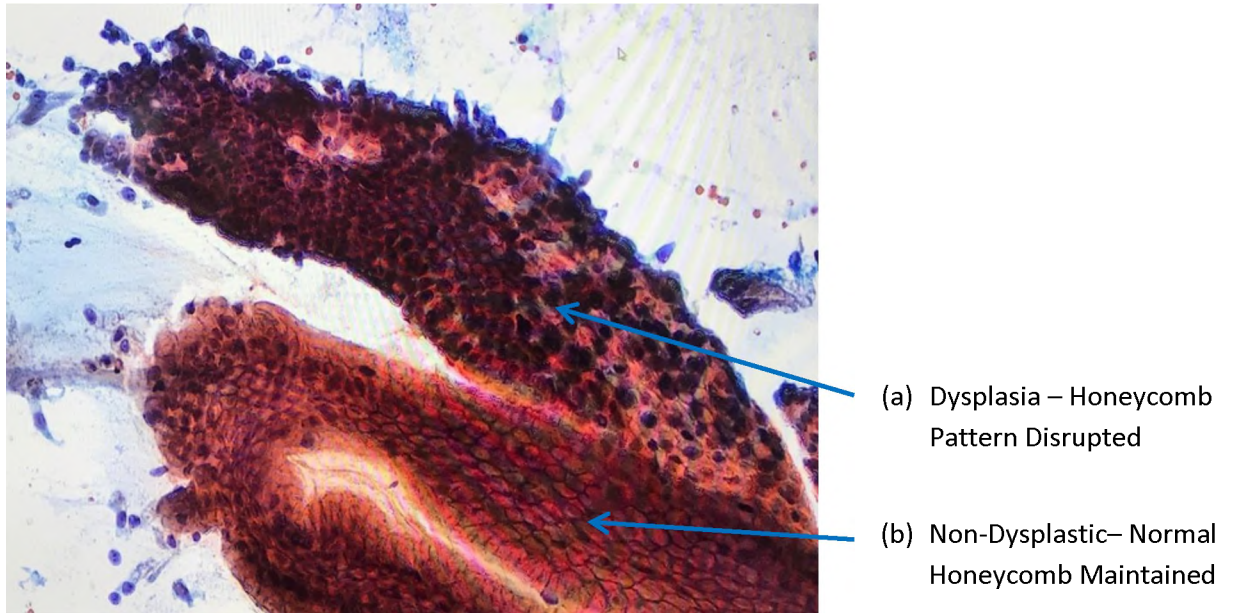**Figure 16. The computer synthesized three dimensional *enface* view of the glandular surface allows definitive identification of dysplastic change.** Regular honeycomb arrangement of cells in the non-dysplastic BE region (b) becomes irregular in the dysplastic region (a). EDF synthesized image of transepithelial brush biopsy of Barrett's esophagus stained with modified Papanicolaou 100X.

2.5   Correlation of forceps biopsy histologic results as an independent measure of dysplastic atypia on transepithelial oral cytology specimens

Transepithelial brush biopsy specimens of squamous epithelium do not display the characteristic honeycomb appearance found in the *enface* view of non-dysplastic glandular tissue. Verification of the accuracy of our proposed method for differentiating between dysplastic and inflammatory atypia in the oral cavity therefore requires a different "gold standard" to verify the presence of dysplasia.

Unlike in Barrett's esophagus, where areas of dysplasia usually do not have any clinically visible or identifiable features, epithelial dysplasia in the oral cavity is characterized by an obvious white or red area of tissue change that is visible under careful examination with a standard white examination light and are known as leukoplakia or erythroplakia respectively.

As a result, the findings of oral transepithelial cytology, specifically, our method of differentiating dysplastic from inflammatory change, can be verified by the findings of a forceps biopsy that was simultaneously taken from the same oral lesion. This is because differentiation of inflammatory from dysplastic cellular atypia on the resultant histological specimen is straightforward, as the architectural changes associated with dysplasia and preserved on the histological specimen are not found in simple inflammation. (Speight)

CHAPTER III

RESULTS

3.1 Chronic Inflammation is associated with Double Strand DNA Breaks (DSBs)

3.1.1 Oral cavity (Squamous)

3.1.1.1 Correlation between a morphologic report of "chronic inflammation" and activation of molecules associated with the detection of and response to DSBs in oral squamous tissue

An unbiased, retrospective chronological data base search of clinical laboratory archives was conducted for transepithelial oral brush cytology of clinically apparent leukoplakias and erythroplakias which were reported as either "Inflammation" or "Negative". Cases reported as "Chronic Inflammation" that did not have a corroborating histology report taken from a simultaneous forceps biopsy of the lesion were excluded. Cases which were reported as having any degree of "dysplasia" on either the oral brush cytology or the contemporaneous scalpel biopsy histology were also excluded. Reports

of "Chronic Inflammation" were based on the presence of the characteristic inflammatory cells.

From this data base search, 20 cases reported as" Chronic Inflammation" based on morphologic criteria and 20 matching control cases reported as "Negative" by the same morphologic criteria were identified.

A cut of the archived cell block from all 40 cases was taken and subjected to IHC for the presence of phosphorylated ATM, phosphorylated CHk2, and H2AX.

All IHC stained specimens were then subjected to neural network based computer assisted morphometric analysis as described in 2.2 above which resulted in a "neural network score" for each stain for each specimen. The average of the neural net scores for each group of specimens organized as positive and negative for Inflammation are shown in Figure 17.

Neural Network Scores	p-ATM (-Inf)	p-H2AX (-Inf)	p-Chk2 (-Inf)	p-ATM (+Inf)	p-H2AX (+Inf)	p-Chk2 (+Inf)
	0.15	0.2	0.1	0.85	0.87	0.95
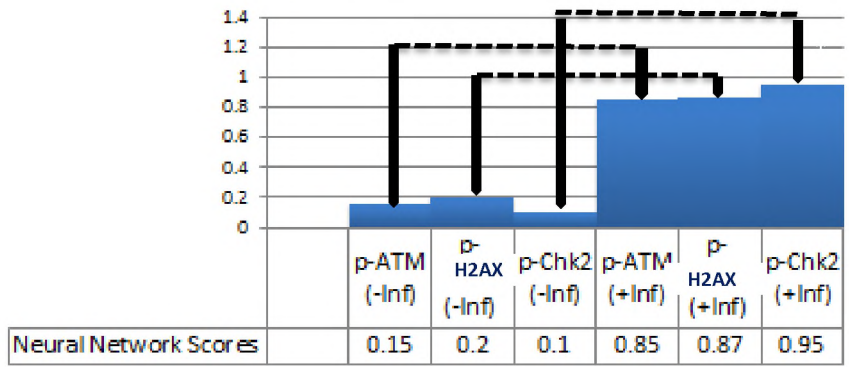
Chronic Inflammation   –   –   –   +   +   +

Figure 17: Phosphorylation of molecules responsible for response to a DNA double strand break (DSB) is correlated with the presence of chronic inflammation in oral squamous epithelium. Dysplasia was absent in these cases. As can be seen, activation of the molecules responsible for the response to a DNA double strand break is correlated with a morphologically based report of chronic inflammation. ▬▬▬▬▬▬▬ = (p<.001)

3.1.1.2 Differentiation between inflammatory and dysplastic atypia in oral squamous tissue

Another unbiased, retrospective chronological data base search of laboratory archives was conducted for oral brush biopsies of clinically apparent leucoplakias and erythroplakias which were reported as "Chronic Inflammation" on transepithelial brush cytology and that also had a histology report taken from a simultaneous scalpel biopsy of the lesion.

From this data base search, 20 cases reported as" Chronic Inflammation" on the transepithelial cytology and also reported a "Negative for Dysplasia" on the contemporaneous scalpel biopsy histology report, and 20 cases reported as "Chronic Inflammation" on the transepithelial cytology and "Positive for Dysplasia" (any degree) on the matching scalpel biopsy histology report were identified.

A cut of the archived cell block from all cases was taken and subjected to IHC for the presence of phosphorylated ATM, phosphorylated Chk2, H2AX, and p53.

All IHC stained specimens were then subjected to the neural network-based computer assisted analysis as described above in 2.2, which resulted in a "neural network score" for both p-Chk2 and p53. The average neural network score for p-Chk2 as compared to the average neural network score for p53, is shown in Figure 18. Inflammatory and dysplastic atypia consistently showed a differential in the ratio between the neural network scoring for p-Chk2 and p53 ($p < 0.5$).

(a) Inflammatory Atypia

Neural Network Scores	p-Chk2	p53
	1.25	0.85

(b) Dysplastic Atypia
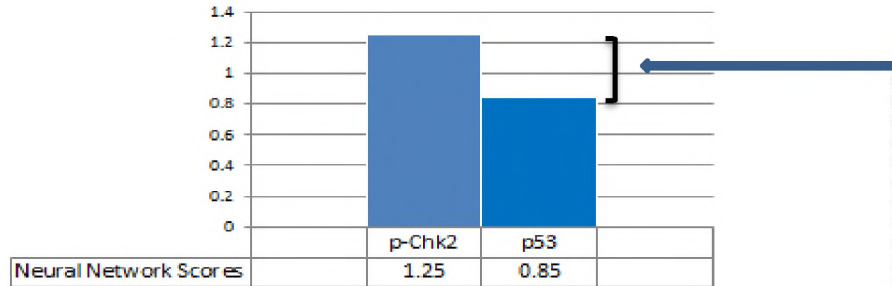
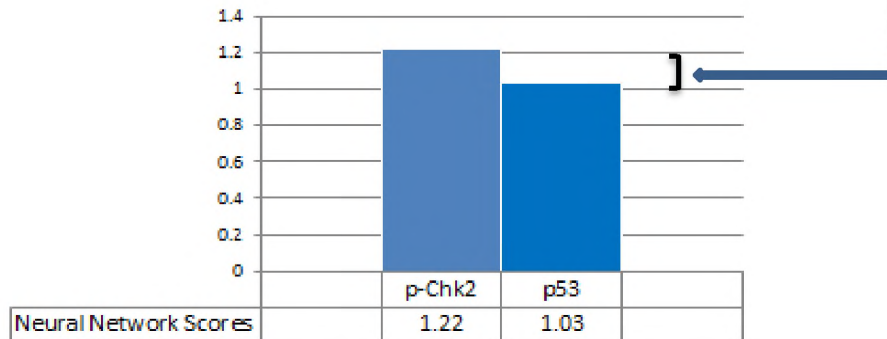| Neural Network Scores	p-Chk2	p53
	1.22	1.03

Figure 18. Neural network scoring of IHC levels identifies squamous dysplasia.   The ratio between the average neural network scores quantifying the IHC levels of p53 and pCHk2 is significantly decreased in dysplasia (b) vs inflammatory atypia (a) in oral squamous epithelium.   -------------- = p <.05

3.1.2 Barrett's Esophagus (Glandular)

3.1.2.1 Correlation between a morphologic report of "chronic inflammation" and activation of molecules associated with the detection of and response to DSBs in the glandular tissue comprising Barrett's esophagus

An unbiased search of clinical laboratory archives was conducted for transepithelial esophageal cytology brushings of segments of Barrett's esophagus which were reported as either "Barrett's esophagus with chronic Inflammation" or "Barrett's esophagus with no report of inflammation. Cases that were reported as having any degree of "dysplasia" on either the transepithelial brush cytology or on a contemporaneous forceps biopsy histology report were excluded. Reports of "Chronic Inflammation" were based on the presence of the characteristic inflammatory cells.

From this data base search, the most recent 25 cases reported as" Barrett's Esophagus with Chronic Inflammation" and the most recent 25 control cases reported as "Barrett's esophagus with no report of Inflammation" were identified.

A cut of the archived cell block from all 40 cases was taken and subjected to IHC for the presence of phosphorylated ATM, phosphorylated CHk2, and p-H2AX.

All IHC stained specimens were then subjected to neural network based computer assisted morphometric analysis as described above in 2.2, which resulted in a "neural network score" for each stain for each specimen. These average neural net scores for the

40 specimens organized as positive and negative for Inflammation are shown in Figure

19.

Neural Network Scores	p-ATM (-Inf)	p-H2AX (-Inf)	p-Chk2 (-Inf)	p-ATM (+Inf)	p-H2AX (+Inf)	p-Chk2 (+Inf)
	0.11	0.25	0.15	0.87	0.8	0.91

Chronic Inflammation   -   -   -   +   +   +

Figure 19: Phosphorylation of the molecules responsible for response to a DNA double strand break is correlated with chronic glandular inflammation. Dysplasia was absent in these cases. As can be seen, activation of the molecules responsible for the response to a DNA double strand break is correlated with a morphologically based report of chronic inflammation in the glandular epithelium of Barrett's esophagus.

- - - - - - - - - - - - - = ($p<.001$)

As can be seen, activation of the molecules responsible for response to a DNA double strand break is correlated with a morphologically based report of chronic inflammation (p <0.001).

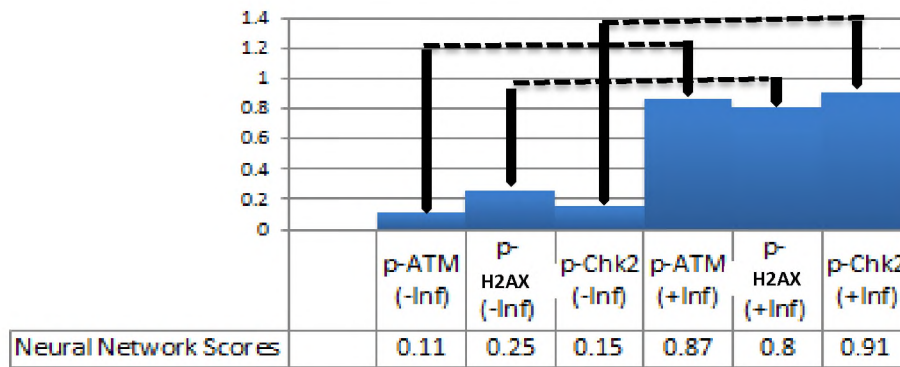### 3.1.2.2   Differentiation between inflammatory and dysplastic atypia in Barrett's esophagus

An unbiased, retrospective search of clinical laboratory archives was conducted for transepithelial cytology brushings of Barrett's esophagus which were reported as "Chronic Inflammation" on transepithelial brush cytology and that also had adequate 3D capture of the *enface* view of the gland so that the presence or absence of dysplasia could be reported.

From this data base search, 20 cases reported as" Chronic Inflammation" on the transepithelial cytology and also reported as "Negative for Dysplasia" based on the 3D *enface* view of the gland, and an equal number of cases reported as "Chronic Inflammation" and Positive for Dysplasia" based on the 3D *enface* view of the gland were identified.

Cuts of the archived cell block from all 40 cases were made and subjected to IHC for the presence of p-CHk2, and p53. These IHC stained specimens were then subjected to neural network based computer scoring as described above in 2.2, which resulted in a "neural network score" for both stains for each specimen. Inflammatory and dysplastic

atypia consistently showed a differential in the ratio between the neural network scoring

for p-Chk2 and p53 (p < 0.5). (Figure 20)

(a) Inflammatory Atypia

Neural Network Scores	p-Chk2	p53	
	1.15	0.75	

(b) Dysplastic Atypia
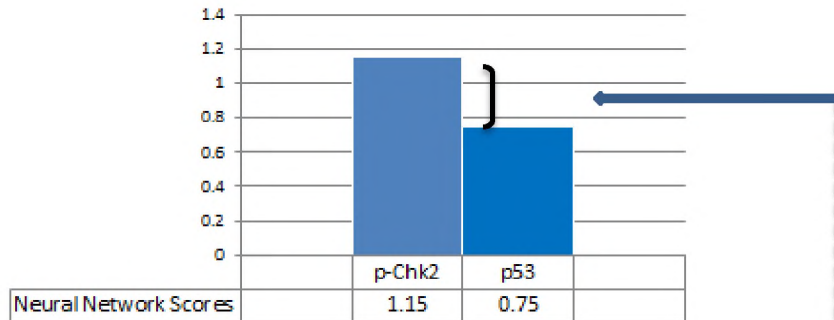
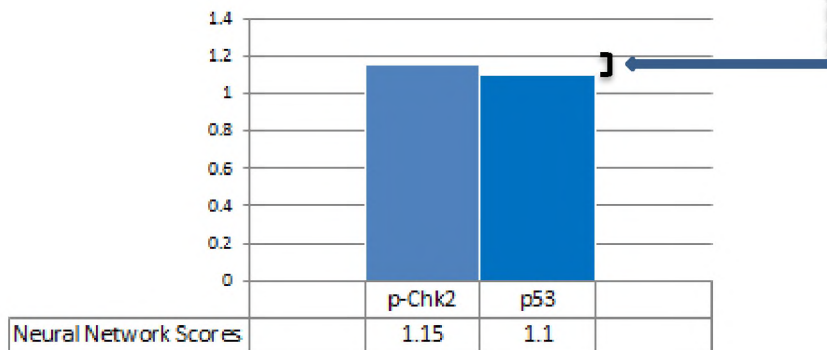| Neural Network Scores	p-Chk2	p53	
	1.15	1.1	

Figure 20: Neural network scoring of IHC levels identifies glandular dysplasia. The ratio between neural network scores quantifying the IHC levels of p53 and pCHk2 is decreased in dysplasia (b) vs inflammatory atypia (a) in glandular specimens obtained from patients with intestinal metaplasia. ―――――――――― = p <.05

3.2. Statistical Analysis

Correlation between a laboratory report of chronic inflammation based on morphology, and the phosphorylation of molecules involved in the detection and repair of DSB's was statistically significant with a $p<.001$ for both squamous (Figure 17) and glandular (Figure 19) epithelia. The average mean neural network score for all three molecules was 0.89 with a standard deviation of 0.12 for the inflammatory squamous tissue vs. an average mean neural network score of 0.15 and a standard deviation of 0.07 for the non-inflammatory squamous tissue controls. For the glandular epithelia the average mean neural network score for all three molecules was 0.86 with a standard deviation of 0.10 for the inflammatory tissue vs. an average mean neural network score of 0.17 and a standard deviation of 0.07 for the non-inflammatory squamous tissue controls

The difference between the ratio of the neural network scores for p53 and p-Chk2 in dysplastic squamous inflammatory epithelium vs. non-dysplastic squamous inflammatory epithelium (Figure 18) was statistically significant ($p<.05$) with mean ratios of 0.68 for inflammatory atypia and 0.84 for dysplastic atypia with standard deviations of 0.2 for both means.

The difference between the ratio of the neural network scores for p53 and p-Chk2 in dysplastic glandular inflammatory epithelium vs. non-dysplastic glandular inflammatory epithelium (Figure 20) was statistically significant ($p<.05$) with mean ratios

of 0.65 for inflammatory atypia and 0.95 for dysplastic atypia and with standard deviations of 0.18 for both means.

Statistical software used Wolfram Mathematica v. 12.0

CHAPTER IV

DISCUSSION

4.1 Overview

The relationship between the presence of chronic inflammation and a propensity

to carcinoma has been noted observationally in the epithelia of numerous body sites, and

several causal mechanisms for this relationship have been suggested.

Regardless of the causation however, their correlation alone has limited the

potential applicability of what has been demonstrated to be the single most effective

intervention to prevent carcinoma- the cytological identification and treatment of

precancerous dysplasia.

Inflammation is a far more common occurrence then the accumulation of mitotic

errors required for the appearance of morphologically recognized dysplasia. The fact that

the morphological appearance of inflammatory atypia can precisely mimic the

morphological appearance of the cellular atypia caused by low grade dysplasia has limited

the effectiveness of cytological screening in almost all body sites in which it has been

attempted. Methods to reliably differentiate between inflammatory and dysplastic cellular atypia have been the focus of molecular and morphologic research without significant success to date.

Due to the almost infinite number of point mutations and gene rearrangements that can lead to precancerous change and cancer, all current diagnoses of dysplasia and cancer are primarily made by their morphologic features. For cytopathology, however, since the mid 1990's morphologic diagnosis is routinely supplemented by molecular testing. This molecular testing is typically implemented through either IHC, flow cytometry, or FISH.

Immunohistochemistry has been demonstrated to be a practical, cost effective method to detect the presence of the activation of molecular pathways responsible for normal cellular differentiation, apoptosis, and the failure to maintain normal differentiation that we refer to as cancer. An advantage of IHC is that unlike flow cytometry, FISH, and genomic or proteomic sequencing, it generally maintains the morphologic appearance of the cell and thus, lends itself to a practical adjunctive diagnostic role. A disadvantage however is that until this study the analysis of IHC was entirely qualitative.

While the actual antigenic response to an IHC antibody is inherently a precise one, the effectiveness of IHC as a test is potentially limited by the non-quantitative nature of its analysis and reporting. Clinical reporting of IHC typically involves a 1-4 subjective impression made by the pathologist of the number and intensity of stained cells.

The potential of precise measurement of IHC levels to add to both our understanding of molecular mechanisms and to the usefulness of clinical reporting of IHC is unknown. In theory, a precise measurement of antigenic response over a large number of cells normalized by the total number of cells in the specimen would result in these two benefits. However, the unavoidable limitations imposed by subjective judgment, human perception and frankly, the fatigue and tedium required to evaluate the stain reaction on hundreds of thousands of epithelial cells and differentiating them from staining artifacts on a slide, have prevented the quantitative potential of IHC from being realized.

This study addressed these limitations of IHC by incorporating quantitative measurement of the total antigenic response on non-artifactual objects. Both the algorithmic and non-algorithmic i.e. "artificial intelligence" image processing and quantification methods employed herein are computationally intensive and were not available until large computer memory capacity and very high processing speeds were recently made available.

This study utilized these recent advances in computer image processing to allow quantification of IHC levels previously not achieved. This quantification in turn allowed us to demonstrate that in two widely varying epithelia, the squamous tissue lining the oral cavity and the glandular tissue comprising Barrett's metaplasia, chronic inflammation is consistently associated with the phosphorylation of molecules responsible for the detection of, and response to, the formation of DNA double strand breaks (DSBs).

This same computer image processing technology also allowed for a precise comparison of the quantification of the molecular markers associated with DSB formation and the presence of p53 resulting in reliable differentiation between inflammatory and dysplastic atypia. Detection of precancerous dysplasia for subsequent treatment or surgical removal has been demonstrated to be the most effective intervention yet developed to prevent cancer.

4.2 Future Directions

The cervical Papanicolaou smear, the excision of abnormally appearing skin moles, and routine screening colonoscopy are the three examples of how programs to screen the population for the presence of precancerous dysplasia can help prevent the development of deadly cancers. One of the reasons why these programs are successful is due to the fact that confounding inflammatory atypia is not a significant obstacle in these particular body sites. The pathologic diagnoses of dysplasia for the uterine cervix, skin, and colon, are therefore typically determined morphologically, and IHC or other molecular tests are not generally required.

However, extending this cancer prevention model to other body sites such as the oral cavity, throat, lung, esophagus, and stomach, where inflammatory cellular atypia that morphologically mimics true dysplasia is an extremely common phenomenon, will likely require more than a morphologic solution. Our data indicate that neural network based

computer image processing of IHC detected activation of molecules involved in DNA damage detection and repair pathways may provide that solution.

Population screening is, by definition, performed on large populations of patients with either no symptoms, or common, usually harmless-appearing signs or symptoms of disease. As such, controlling the cost of screening is an important factor.

One advantage of IHC over other molecular tests is its relatively low cost and low technological threshold in the laboratory. Low cost is particularly important for implementation in South Asia, where in many countries including India, oral cancer is one of the most frequent causes of cancer death. Our study showed that neural network based quantification of IHC levels of pChk2 and p53 can be utilized to distinguish between inflammatory and dysplastic change. While IHC staining for p53 IHC is commonly used and therefore inexpensive, IHC staining for pCHk2 is not. It can be expected that neural network based quantification of the IHC levels of the other two molecular markers of Double Strand Breaks found in our study to be associated with inflammation i.e. ATM and H2AX can also be compared to neural network based quantification of p53 to distinguish inflammatory from dysplastic atypia.

Future research will test the conclusions of this study on these two additional markers of Double Strand DNA breaks with the goal of selecting the most reproducible and most economically implemented of them to correlate with neural network quantification of the level of p53.

4.3 Conclusions

Utilizing a combination of algorithmic and artificial intelligence-based computer image analysis of IHC levels, we find that phosphorylation of molecular markers associated with DSBs is consistently and strongly correlated with non-dysplastic inflammatory atypia in both squamous (oral cavity) and glandular (Barrett's metaplasia) epithelia. Using these same image analysis methods, we further show that quantitative immunohistochemistry of the ratio of the level of pChk2 and p53 can reliably distinguish between inflammatory and dysplastic cellular atypia.

REFERENCES

Ahn J, Xia T, Konno H, et al. Inflammation-driven carcinogenesis imediated through STING; Nature Communications. 2014;5:5166.

Anandasabapathy S, Sontag S, Graham DY, et al. Computer-assisted brush-biopsy analysis for the detection of dysplasia in a high-risk Barrett's esophagus surveillance population. Dig Dis Sci. 2011;56:761-6.

Barash H, R Gross E, Edrei Y, et al. Accelerated carcinogenesis following liver regeneration is associated with chronic inflammation-induced double-strand DNA breaks. Proc Natl Acad Sci USA. 2010;107(5):2207-12.

Bartkova J, Horejsí Z, Koed K et al. DNA damage response as a candidate anti-cancer barrier in early human tumorigenesis Nature. 2005;434(7035):864-70.

Brooks CL, Gu W. p53 regulation by ubiquitin. FEBS Lett. 2011;585(18):2803-9.

Cao L, Kim S, Xiao C et al. ATM–Chk2–p53 activation prevents tumorigenesis at an expense of organ homeostasis upon Brca1 deficiency. EMBO J. 2006;25(10): 2167–2177.

Contino G, Vaughan TL, Whiteman D, Fitzgerald RC. The Evolving Genomic Landscape of Barrett's Esophagus and Esophageal Adenocarcinoma. Gastroenterology. 2017;153(3):657-673.

Creamer B, Shorter RG, Bamforth J. The turnover and shedding of epithelial cells. I. The turnover in the gastro-intestinal tract. Gut. 1961 ;2:110-8.

Dinarello CA. Historical insights into cytokines. Eur J Immunol. 2007;37 Suppl 1:S34-45.

Falk GW. Cytology in Barrett's esophagus. Gastrointest Endosc Clin N Am. 2003;13(2):335-48.

Folsom TC, White CP, Bromer L, Canby HF, Garrington GE. Oral exfoliative study. Review of the literature and report of a three- year study. Oral Surg Oral Med Oral Pathol. 1972;33:61-74.

Gibbins JR. Metabolic requirements for epithelial migration as defined by the use of metabolic inhibitors in organ culture. Exp Cell Res. 1972;71(2):329-37.

Gomes M, Teixeira AL, Coelho A et al. The role of inflammation in lung cancer. Adv Exp Med Biol. 2014;816:1-23.

Gross SA, Smith MS, Kaul V, US Collaborative WATS³ᴰ Study Group. Increased detection of Barrett's esophagus and esophageal dysplasia with adjunctive use of wide-area transepithelial sample with three-dimensional computer-assisted analysis (WATS). United European Gastroenterlogy Journal. 2018;6(4):529-535.

Gupta RB, Harpaz N, Itzkowitz S, et al. Histologic inflammation is a risk factor for progression to colorectal neoplasia in ulcerative colitis: a cohort study. Gastroenterology. 2007;133(4):1099-105.

Hayes RL, Berg GW, Ross WL. Oral cytology: its value and its limitations. J Am Dent Assoc. 1969;79:649-57.

Hussain SP, Harris CC. Inflammation and cancer: an ancient link with novel potentials. Int J Cancer. 2007;121:2373–2380.

Iype EM, Pandey M, Mathew A, Thomas G, Sebastian P, Nair MK. Oral cancer among patients under the age of 35 years. J Postgrad Med. 2001;47(3):171-6.

Jackson SP, Bartek J. The DNA-damage response in human biology and disease. Nature. 2009;461(7267): 1071–1078.

Jeggo PA and Lobrich M. DNA double-strand breaks: Their cellular and clinical impact? Oncogene. 2007;26:7717–7719.

Johanson JF, Frakes J, Eisen D. Computer-assisted analysis of abrasive transepithelial brush biopsies increases the effectiveness of esophageal screening: a multicenter prospective clinical trial by the EndoCDx Collaborative Group. Dig Dis Sci. 2011;56:767-72.

Kalisperati P, Spanou E, Pateras IS, et al. Inflammation, DNA Damage, *Helicobacter pylori* and Gastric Tumorigenesis. Front Genet. 2017;8:20.

Kanda Y, Osaki M, Okada F. Chemopreventive strategies for inflammation-related carcinogenesis: current status and future direction. Int J Mol Sci. 2017; 18(4): 867.

Kang J, Ferguson D, Song H et al. Functional interaction of H2AX, NBS1, and p53 in ATM-dependent DNA damage responses and tumor suppression. Mol Cell Biol. 2005;25(2):661–670.

Kawanishi S, Hiraku Y. Oxidative and nitrative DNA damage as biomarker for carcinogenesis with special reference to inflammation. Antioxid Redox Signal. 2006;8 (5-6):1047-58.

Kerkhof M, van Dekken H, Steyerberg EW, et al. Grading of dysplasia in Barrett's oesophagus: substantial interobserver variation between general and gastrointestinal pathologists. Histopathology. 2007;50 (7):920-7.

Kiraly O, Gong G, Olipitz W, Muthupalani S, Engelward BP. Inflammation-induced cell proliferation potentiates DNA damage-induced mutations in vivo. PLoS Genet. 2015;11 (2):e1004901.

Koss, LG. Diagnostic cytology and its histologic basis. Philadelphia: J.B. Lippincott, Co., 1961.

Kumaravel A, Lopez R, Brainard J, Falk GW. Brush cytology vs. endoscopic biopsy for the surveillance of Barrett's esophagus. Endoscopy. 2010;42(10):800-5.

Mango LJ, Radensky PW. Interactive neural-network-assisted screening. A clinical assessment. Acta Cytol. 1998;42(1):233-45.

Martincorena I, Raine KM, Gerstung M, et al. Universal Patterns of Selection in Cancer and Somatic Tissues. Cell. 2017;171(5):1029-1041.

Mehrotra R, Mishra S, Singh M. The efficacy of oral brush biopsy with computer-assisted analysis in identifying precancerous and cancerous lesions. Head Neck Oncol. 2011;3:39.

Mittal M, Siddiqui MR, Tran K, Reddy SP, Malik AB. Reactive oxygen species in inflammation and tissue injury. Antioxid Redox Signal. 2014;20(7):1126-67.

Montgomery E, Goldblum JR, Greenson JK, et al. Dysplasia as a predictive marker for invasive carcinoma in Barrett esophagus: a follow-up study based on 138 cases from a diagnostic variability study. Hum Pathol. 2001;32(4):379-88.

Murata M, Thanan R, Ma N, Kawanishi S. Role of nitrative and oxidative DNA damage in inflammation-related carcinogenesis. J Biomed Biotechnol. 2012;2012:623019.

Naini BV, Souza RF, Odze RD. Barrett's esophagus: a comprehensive and contemporary review for pathologists. Am J Surg Pathol. 2016;40(5):e45-66.

National Institutes of Health. Cervical cancer. Fact Sheet. 2010. https://report.nih.gov/nihfactsheets/Pdfs/CervicalCancer(NCI).pdf

Ohnishi S, Ma N, Thanan R, et al. DNA damage in inflammation-related carcinogenesis and cancer stem cells. Oxid Med Cell Longev. 2013;2013:387014.

Paderno A, Morello R, Piazza C.Acta Otorhinolaryngol Ital. 2018;38(3):175–180.

Paull TT, Deshpande RA. The Mre11/Rad50/Nbs1 complex: recent insights into catalytic activities and ATP-driven conformational changes. Exp Cell Res. 2014;329(1):139-47.

O'Brien MJ, Winawer SJ, Zauber AG, et al. The National Polyp Study. Patient and polyp characteristics associated with high-grade dysplasia in colorectal adenomas. Gastroenterology. 1990;98(2):371-9.

Rivlin N, Brosh R, Oren M, Rotter V. Mutations in the p53 tumor suppressor gene: important milestones at the various steps of tumorigenesis. Genes Cancer. 2011;2(4):466-74.

Rogakou EP, Pilch DR, Orr AH, et al. DNA double-stranded breaks induce histone H2AX phosphorylation on serine 139. J Biol Chem. 1998;273(10):5858-68.

Rustgi AK, El-Serag HB. Esophageal carcinoma. N Engl J Med. 2014;371:2499-2509.

Rybak P, Hoang A, Bujnowicz L, et al. Low level phosphorylation of histone H2AX on serine 139 (γH2AX) is not associated with DNA double-strand breaks. Oncotarget. 2016;7(31):49574-49587.

Sandler H. Cytological screening for early mouth cancer. Cancer. 1962;15:1119-1124.

Scarpa M, Castagliuolo I, Castoro C, et al. Inflammatory colonic carcinogenesis: a review on pathogenesis and immunosurveillance mechanisms in ulcerative colitis. World J Gastroenterol. 2014;20 (22):6774-85.

Scheifele C, Schmidt-Westhausen AM, Dietrich T, Reichart PA. The sensitivity and specificity of the OralCDx technique: evaluation of 103 cases. Oral Oncol. 2004;40(8):824-828.

Sciubba JJ for the U.S. Collaborative OralCDx Study Group. Improving detection of precancerous and cancerous oral lesions. Computer-assisted analysis of the oral brush biopsy. J Am Dent Assoc. 1999;130(10):1445-57.

Sciubba JJ , Larian, B. Oral squamous cell carcinoma: early detection and improved 5-Year survival in 102 patients. 2018 General Dentistry. Gen Dent. 2018;66(6):e11-e16.

Serra J. Image Analysis and Mathematical Morphology. Academic Press, London. 1982

Sharma P. Review article: emerging techniques for screening and surveillance in Barrett's oesophagus. Aliment Pharmacol Ther. 2004;20 Suppl 5:63-70; discussion 95-6.

Shaheen N, Ransohoff DF. Gastroesophageal reflux, Barrett esophagus, and esophageal cancer: scientific review. JAMA. 2002;287(15):1972–1981.

Siegel RL, Miller KD, Jemal A. Cancer statistics, 2019. Cancer CA Cancer J Clin. 2019;69:7-34.

Smith MS. The Role of Brush Biopsy in the Management of Barrett Esophagus. Gastroenterology & Hepatology. 2016;12, Issue 11. http://www.gastroenterologyandhepatology.net/archives/november-2016/the-role-of-brush-biopsy-in-the-management-of-barrett-esophagus/

Smith MS, Ikonomi E, Bhuta R, et al. and the US Collaborative WATS Study Group. Wide-area transepithelial sampling with computer-assisted 3-dimensional analysis (WATS) markedly improves detection of esophageal dysplasia and Barrett's esophagus: analysis from a prospective multicenter community-based study. Dis Esophagus. 2018 Dec 12. doi: 10.1093/dote/doy099.

Spechler SJ. Clinical practice. Barrett's Esophagus. N Engl J Med. 2002;346:836-42.

Spechler SJ, Souza RF. Barrett's esophagus. N Engl J Med. 2014; 371:836-845.

Speight PM. Update on oral epithelial dysplasia and progression to cancer. Head Neck Pathol. 2007;1(1):61-6

Svirsky JA, Burns JC, Carpenter WM et al. Comparison of computer-assisted brush biopsy results with follow-up scalpel biopsy and histology. Gen Dent. 2002;50:500-3.

Thanan R, Pairojkul C, Pinlaor S, et al. Inflammation-related DNA damage and expression of CD133 and Oct3/4 in cholangiocarcinoma patients with poor prognosis. Free Radic Biol Med. 2013; 65:1464-1472.

Tomasetti C, Li L, Vogelstein B. Stem cell divisions, somatic mutations, cancer etiology, and cancer prevention. Science. 2017:35(6331):1330-34.

Triantafillidis JK, Nasioulas G, Kosmidis PA. Colorectal cancer and inflammatory bowel disease: epidemiology, risk factors, mechanisms of carcinogenesis and prevention strategies. Anticancer Res. 2009;29(7):2727-37.

Toller IM, Neelsen KJ, Steger M, et al. Carcinogenic bacterial pathogen Helicobacter pylori triggers DNA double-strand breaks and a DNA damage response in its host cells. Proc Natl Acad Sci U S A. 2011;108(36):14944-9.

van Gerven M, Bohte S. Artificial neural networks as models of neural information processing. Published in Frontiers of Computational Neuroscience. 2018.

Vennalaganti PR, Kaul V, Wang KK, et al. Increased detection of Barrett's esophagus-associated neoplasia using Wide-Area Trans-epithelial Sampling: A multicenter, prospective, randomized trial. Gastrointest Endosc. 2018;87(2):348-355.

Vennalaganti PR, Naag Kanakadandi V, Gross SA, et al. Inter-Observer agreement among pathologists using Wide-Area Transepithelial Sampling with computer-assisted analysis in patients with Barrett's esophagus. Am J Gastroenterol. 2015;110:1257-60.

Visrodia K, Singh S, Krishnamoorthi R, et al. Magnitude of missed esophageal adenocarcinoma after Barrett's esophagus diagnosis: A systematic review and meta-analysis. Gastroenterology. 2016;150(3):599-607.

Vogelstein B, Kinzler KW. The multistep nature of cancer. Trends Genet. 1993;9 (4):138-41.

Wani S, Falk GW, Post J, et al. Risk factors for progression of low-grade dysplasia in patients with Barrett's esophagus. Gastroenterology. 2011;141:1179–186, 1186.e1.

Weinberg OK, Gibson CJ, Blonquist TM, et al. Association of mutations with morphological dysplasia in *de novo* acute myeloid leukemia without 2016 WHO Classification-defined cytogenetic abnormalities. Haematologica. 2018;103(4):626-633.

Williams AB, Schumacher B. p53 in the DNA-Damage-Repair Process. Cold Spring Harb Perspect Med. 2016;6(5).

Zannini L, Delia D, Buscemi G. CHK2 kinase in the DNA damage response and beyond. J Mol Cell Biol. 2014;6(6):442-57.